Simulating Transonic Buffet Aerodynamics for the Boeing Transonic Truss-Braced Wing Aircraft

Oliver M. F. Browne*, Daniel Maldonado†, Jeffrey A. Housman‡, and Jared C. Duensing§
NASA Ames Research Center, Moffett Field, CA 94035

William E. Milholen¶
NASA Langley Research Center, Hampton, VA 23681

The flow past the Boeing Transonic Truss-Braced Wing (TTBW) aircraft is simulated with a Hybrid Reynolds-Averaged Navier Stokes Large-Eddy Simulations (HRLES) turbulence modeling approach to study transonic buffet onset and evaluate the predictive capability of the numerical approach. All simulations used structured overset curvilinear grids for the free-air configuration, with all simulations performed using the Launch, Ascent, and Vehicle Aerodynamics (LAVA) computational framework. Aerodynamic loads and surface pressure obtained from the HRLES solutions are compared to results from unsteady RANS (URANS) and experiments conducted at NASA Ames 11-by 11-Foot Transonic Wind Tunnel. Overall good agreement is obtained in the predicted loads and surface pressure. Unsteady pressure data from HRLES and URANS simulations is utilized to compute power spectral density (PSD) to predict transonic buffet onset and compared to the Kulite data obtained from the experiment. Comparisons of the PSD spectrum also show reasonable agreement with the wind tunnel data, with HRLES and URANS predicting buffet onset at a slightly earlier angle-of-attack than the experiment.

I. Introduction

The Transonic Truss-Braced Wing (TTBW) aircraft concept (shown in Fig. 1) is a design that NASA and Boeing are collaborating to develop which contains advancements in technology that has the potential to improve fuel efficiency for commercial aircraft. The thinner and truss-braced wing has a longer span and reduced wing sweep compared to conventional airliners which can reduce the amount of drag originating from wing tip vortex formation (*i.e.* drag due to lift) and the smaller wing chord would allow for natural laminar flow control to be employed to reduce friction drag. The unconventional configuration of the TTBW which includes a high aspect ratio wing, in addition to wing and jury struts, leads to complex flow phenomena such as *transonic buffet*, shock induced separated flow, and a turbulent wake. The phenomenon of *transonic buffet* is an instability characterized by self-sustained low-frequency oscillations of the shock on the upper surface of the wing which arises when there is shock induced boundary-layer separation due to interactions between the shock and the turbulent boundary-layer. This can result in unsteady loading on the aircraft wings which can cause fatigue failure. Buffet will occur under certain flight conditions such as with increasing Mach number or angle-of-attack and therefore represents an important aspect which limits the operational flight envelope. Hence, accurate predictions of buffet onset are an important milestone for the TTBW.

Current industry best practices tend to employ Reynolds-Averaged Navier-Stokes (RANS)-based computational fluid dynamics (CFD) analysis for buffet onset prediction. However, to accurately predict the onset of buffet and the development of the separated flow, more accurate scale resolving CFD simulations may be required. The recent High Lift Prediction Workshop 4 (HLPW4) further highlighted that steady-state RANS approaches struggle to accurately predict the aerodynamic loads at $C_{L,\max}$ when there were large regions of separated flow on the wing of the NASA High-Lift Common Research Model (CRM-HL)[1]. Scale-resolving simulation approaches such as wall-modelled Large-Eddy Simulations (WMLES)[2–4] and hybrid RANS/LES (HRLES)[5] showed more promise and tended to predict $C_{L,\max}$ within the 2% accuracy requirement proposed within *Certification by Analysis* (CbA)[6]. As the role of

*Science and Technology Corp., AIAA Senior Member, oliver.m.browne@nasa.gov
†Computational Aerosciences Branch, AIAA Member, daniel.maldonado@nasa.gov
‡Computational Aerosciences Branch, AIAA Senior Member, jeffrey.a.housman@nasa.gov
§Computational Aerosciences Branch, AIAA Member, jared.c.duensing@nasa.gov
¶Configuration Aerodynamics Branch, AIAA Senior Member, william.e.milholen@nasa.gov



(a) (b)

Fig. 1 a) Concept image of NASA/Boeing Transonic Truss-Braced Wing aircraft (credit: NASA), and b) a photograph of a model of the Transonic Truss-Braced Wing aircraft installed for testing in the Unitary Plan Wind Tunnel 11-by 11-foot TWT at NASA Ames Research Center (credit: NASA).

CFD advances beyond design and optimization and towards CbA in an attempt to alleviate the high financial burden of wind tunnel and flight testing, there is growing interest in expanding the scope of high-fidelity numerical modeling to target regions of the flight envelope characterized by large regions of separated flows. Within the framework of CbA, it is stipulated that the unsteady aerodynamic loads need to be computed including the effect of separated flows and shock/boundary-layer interactions while also predicting buffet onset within a speed of 3 knots of the validation data. At the very least this would require unsteady RANS (URANS) simulations or, more likely, moving towards time accurate scale-resolving simulations to fulfill this criteria.

The development of the flow instability *transonic buffet* on both two-dimensional airfoils (*e.g.* NACA0012[7], OAT15A[8–10]) and three-dimensional wings (*e.g.* High-Speed Common Research Model (CRM-HS)[11–14], [15]) has been studied with both HRLES and WMLES in recent years. Generally, both approaches show improvements over steady-state RANS computations in terms of the predicted shock positions, although HRLES studies that employed Delayed Detached Eddy Simulations (DDES)[16] have shown a tendency to predict the shock further upstream than experiment and a larger separated region behind the shock. Several authors [14, 17] have proposed modifications to the HRLES shielding function to improve the accuracy the predicted shock location. The aim of this paper is to investigate the predictive capability of HRLES for buffet onset on the TTBW.

Simulations reported in this paper were performed using the structured curvilinear overset Navier-Stokes solver within the Launch, Ascent, and Vehicle Aerodynamics (LAVA) computational framework [18]. The rest of the paper it organized as follows: the numerical modeling approach is outlined in Sec. II, background on the wind tunnel experiments is detailed in Sec. III, simulations results are provided in Sec. IV, and the conclusions and future work are discussed in Sec. V.

II. Numerical Modeling Approach

A. Turbulence Modeling Approach

The HRLES approach employed in this work is the Zonal Detached Eddy Simulation (ZDES) 2020 mode 2 Enhanced Protection (EP) [17] method. The ZDES2020 mode 2 EP method builds upon and attempts to alleviate the shortcomings

of previous iterations of automatic shielding functions developed (*e.g.* Delayed Detached Eddy Simulations, DDES2006 [16] and ZDES2012 mode 2 [19]), with an improved shielding function f_d that should better protect the boundary-layer by staying in RANS mode ($f_d = 0$) for attached flows even in the limit of small Δ/δ_{bl}. Earlier DDES approaches are prone to prematurely going into LES mode ($f_d = 1$) despite the lack of LES (scale resolving) local mesh resolution. This sudden loss of modeled-stress which is not compensated for by any resolved content (resolved Reynolds stress) leads to the well known phenomenon called modeled stress depletion. The ZDES2020 mode 2 EP has previously been validated and used in LAVA[5, 11, 20] and the reader is referred to prior publications[21, 22] for further implementation-specific details. The maximum edge length for a grid-cell serves as the local length scale used in the LES SGS closure.

The Reynolds averaged Navier-Stokes equations are developed using Favre averaging which results in a Reynolds stress tensor which must be modeled to close the governing system of equations. For this paper, the Spalart-Allmaras (SA)[23] turbulence model is the primary turbulence closure being investigated. The SA-neg[24] variant of the model, which modifies the SA equation for pseudo eddy viscosity $\tilde{\nu} < 0$, is the formulation employed but it is referred to as solely SA, for brevity, for the rest of the paper. The SA model is employed with a low-Reynolds number correction[25], which attempts to improve the early development of the boundary layer when the effective Reynolds number is low, and the compressibility correction[26], which was shown to be important for predicting buffet using URANS by Crouch *et al.*[27]. The URANS simulations shown in this paper use the same SA closures.

B. Numerical Discretization

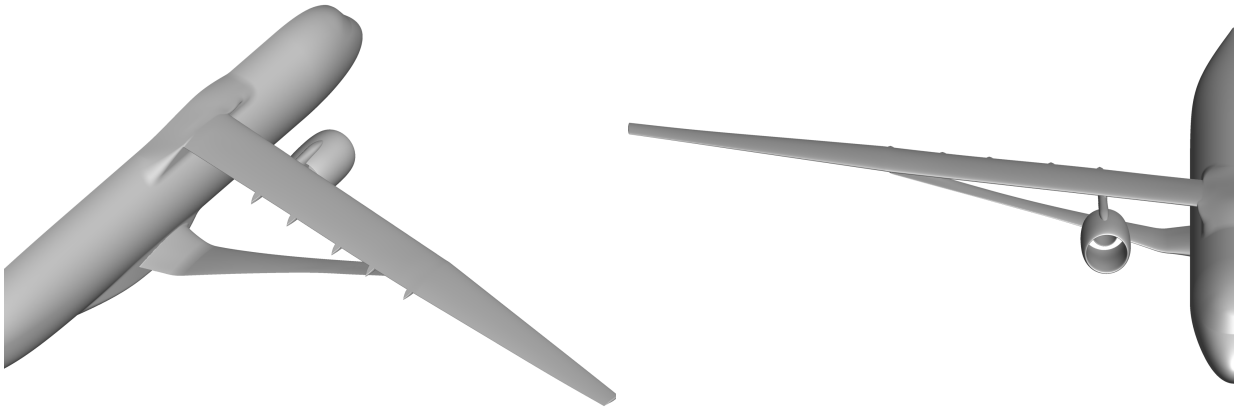
High-order accurate low dissipation finite-difference schemes have been shown to be an accurate and efficient strategy for turbulence resolving simulations using LAVA[21, 22, 28, 29]. A thorough study comparing several high-order finite difference methods on Cartesian grids within the LAVA framework was reported previously[30]. Results from this study indicated that high-order Weighted Essentially Non-Oscillatory (WENO) schemes[31] performed well in both resolution (Points-Per-Wavelength PPW), shock capturing, and robustness under harsh flow conditions. A natural extension of finite-difference WENO schemes to curvilinear grids are the high-order Weighted Compact Nonlinear Schemes (WCNS)[32].

An updated approach, denoted Hybrid Weighted Compact Nonlinear Scheme (HWCNS) [33–35], allows for up to third/fourth-order accuracy using a five-point stencil by combining blended third- and fourth-order interpolation with a fourth-order hybrid central difference operator which utilizes fluxes at both the nodes and mid-points. The blending of an upwind biased and pure central variable reconstruction [36], has been generalized by the authors to variable-order interpolation. Finally, a masking of the blended interpolation (100% 3rd order upwind, 0% 4th order central) is performed near stencils containing overset fringe points for robustness and to reduce numerical artifacts which may occur near overset boundaries using low dissipation schemes. The standard HLL numerical flux is utilized for the convective terms [37]. For time integration, a BDF2 discretization is used in physical time, along with pseudo-time embedding and ILU(1) preconditioned GMRES (see Ref. [38] for more details).

C. Curvilinear Overset Grid

A visualization of the full scale TTBW model that is simulated in this paper is provided in Fig. 2. The semi-span configuration based on experiment model C139 that includes the fuselage, main wing, flap track fairings, nacelle and pylon and a strut. The C139 model does not include the jury strut or the tail surfaces. All the surfaces of TTBW have a no-slip boundary conditions applied and a symmetry boundary condition is applied at the $y = 0$ plane as we are simulating the free air configuration.

Three curvilinear overset grids were generated, namely, a coarse, medium and fine grid. The details of the grids is given in Table 1 and a spanwise slice of the curvilinear grid system in shown in Fig. 3. The medium mesh was generated by doing a 1.4× global refinement of the coarse grid. The fine grid was generated by taking the coarse grid and refining only the upper surface on the main wing by 2.8× and the rest of the grid system remained at the coarse grid level. This was to keep the overall cell count down on the fine grid and a grid refinement study had not shown significant mesh sensitivities on the strut and fuselage. The grids were designed with targeted $y^+ \leq 1$ at the wall and generated specifically for HRLES scale resolving simulations with typically low aspect grid cells away from the wall in regions that are expected to be in LES mode. The wing upper-surface grids start at typical RANS-grid stretching ratios and quickly reduce to values near 1.05 away from the wall to better support LES flow.



(a) perspective view (b) front view

Fig. 2 Full scale semispan TTBW model.

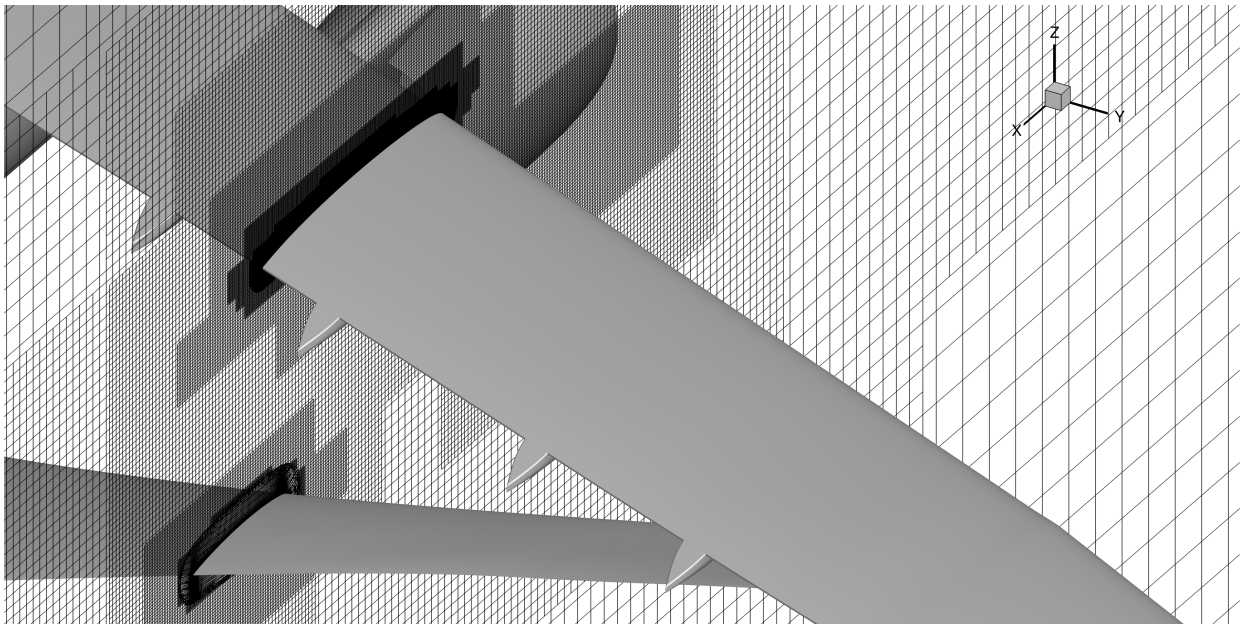


Fig. 3 Spanwise slice showing curvilinear overset grid used for HRLES and URANS simulations.

Table 1 Description of the HRLES and URANS grids used for full scale TTBW simulations.

		Wing Upper Surface				
Name	Solve Points	Δx at $0.5x/c$ (mm)	Δy at $0.5x/c$ (mm)	Stretching Ratio	Target y^+	Δt (s)
Coarse	99.3M	0.024	0.024	1.25	1.0	1e-4
Medium	228.9M	0.0176	0.0176	1.12	1.0	7.14e-05
Fine	397.3M	0.0083	0.0083	1.085	1.0	5e-5

III. Comparison Experimental Data

Figure 1(b) shows the new 9% scale semi-span model of the Subsonic Ultra Green Aircraft Research (SUGAR) M=0.8 TTBW configuration mounted in the test section of the NASA Ames 11-by 11-Foot Transonic Wind Tunnel. The

model was designed and fabricated by Boeing to explore the high-speed buffet onset characteristics of the configuration, and to expand the existing stability and control database (Ref. [39, 40]). Consistent with general semi-span model testing techniques, the tail surfaces were not included. It should also be noted that the jury strut was not included in the testing, due to model scale and loads expected in the testing. A successful four-week test was completed in February 2022 in partnership with Boeing as part of the SUGAR Phase V contract.

The centerline of the fuselage was offset from the tunnel floor approximately 1.0 inch using a metric standoff, while the slots in the tunnel floor were closed using facility supplied blanking plates to create a smooth solid floor for the test section. The slots on the remaining three walls were left open in their usual state to minimize wall interference effects. The gap between the floor and standoff was nominally 0.25 inches, and a series of keel dam flow blockers (Ref. [41]) were designed by Boeing using Navier-Stokes CFD tunnel simulations to minimize the flow under the model, with the goal of replicating the flow over a full-span model. The gap between each keel dam and the local tunnel floor was approximately 0.050 in. The wing/fuselage fairing was also modified to insure the semi-span model would adequately replicate the spanwise lift distribution, including the location of the inboard wing shock wave; critical features for evaluating the high-speed buffet onset mechanisms. The model was fabricated to a jig-shape that would aeroelastically deform to the $1-g$ cruise shape at a tunnel condition of $M_\infty = 0.80$, $C_L = 0.695$, and $Re_{c_{\text{MAC}}} = 5.18 \times 10^6$. It should be noted that model deformations were not measured during the test as a new technique was in development. The test team did weigh the option of using an externally sourced deformation measurement system. However, past experience of testing the smaller and more flexible 4.5% scale full-span $M = 0.8$ TTBW model in the same tunnel had verified the model jig-shape design/fabrication methods. Future CFD modeling efforts by NASA will explore the effects of the predicted model deformations.

The tunnel testing covered a broad range of test conditions with a Mach number range of $0.20 - 0.92$ and a mean chord Reynolds number range of 2.2×10^6 to 6.58×10^6. Aerodynamic forces and moments were measured using the floor mounted 5-component ARC-11-30K balance which was recalibrated prior to the test. The force and moment data was corrected for wall interreference effects using the TWICS method. Several boundary layer trip locations were studied using appropriately sized trip dots, with wing trip locations ranging from $5\% - 40\%$ x/c, while the strut trip location was 10% x/c. The model was well instrumented with 480 static pressure taps, with the spanwise locations on the wing and strut shown in Fig. 4(a). The instrumentation also included strain gauges, accelerometers, and unsteady pressure transducers (Kulites) geared towards characterizing unsteady aerodynamics that would relate to buffet onset. The locations of the Kulites on the wing and strut are illustrated in Fig. 4(b) and 4(c). The test demonstrated very good data repeatability exemplified by the drag coefficient having a statistical variation of $2\sigma = 1.70$ counts, for attached flow (before pitch break) at $M_\infty = 0.80$ and $Re_{c_{\text{MAC}}} = 5.18 \times 10^6$.

IV. Results and Discussion

In this section, the free air configuration results from the URANS and scale resolving CFD simulations performed with a HRLES turbulence modeling approach are presented. The numerical results are compared with experimental data from the Unitary Plan Wind Tunnel 11-by 11-foot TWT at NASA Ames Research Center. The URANS and HRLES are simulated in a free air configuration (1-g shape) and compared with a set of corrected experimental wind tunnel results. The correction takes into account the in-tunnel effects such as the floor boundary-layer, blockage effects from tunnel walls *etc*. As mentioned in Sec. III, the wind tunnel model featured a modified wing/fuselage fairing to attempt to replicate the free air shock location while in the CFD we use the original TTBW wing/fuselage fairing. Fig. 4 shows the locations on the TTBW aircraft that time averaged (Fig. 4(a)) and unsteady (Fig. 4(b) and 4(c)) surface pressures were recorded in the simulations to allow for comparison with the experimental data.

Table 2 Freestream conditions and parameters for TTBW CFD simulations.

Condition	Value
Mean Aerodynamic Chord, c_{MAC} (m)	2.8013
Moment Reference Center (m)	(20.9011,0.0,7.2926)
Mach Number, M_∞	0.8
Reynolds Number, $Re_{c_{\text{MAC}}}$	5.2 M
Reference Static Temperature, T (K)	270

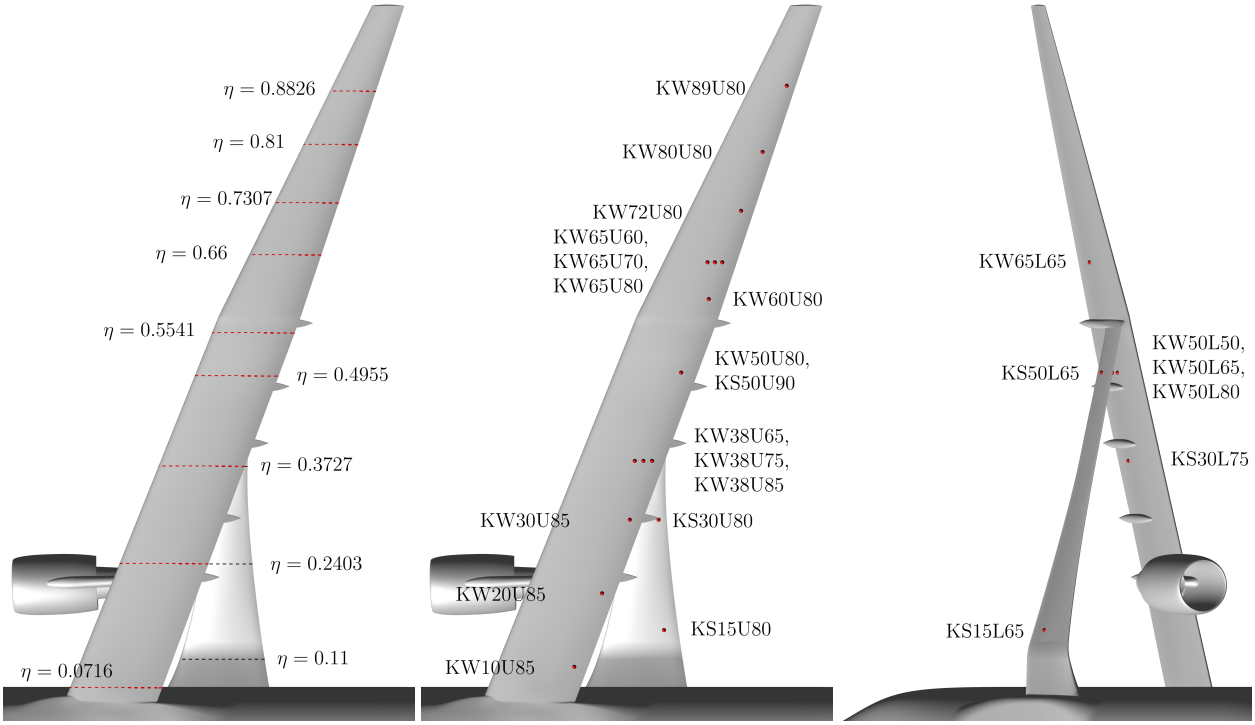
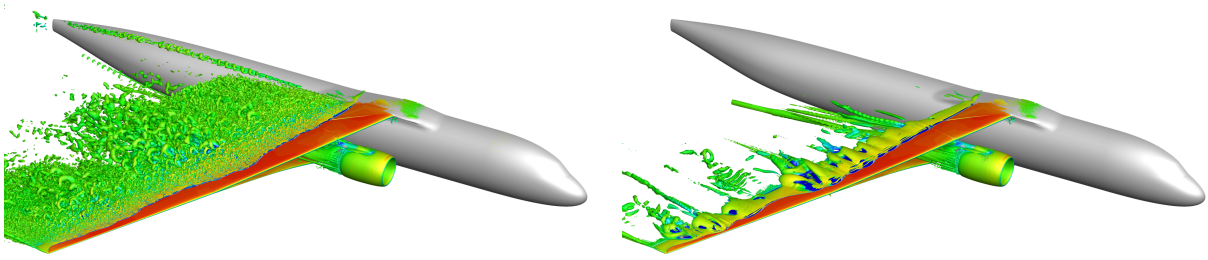


Fig. 4 A schematic of the TTBW test article that provides the locations where time averaged (spanwise slices) pressure and unsteady (probes) pressure was recorded.

The flow past the TTBW aircraft (configuration C139) is simulated with HRLES for $M_\infty = 0.8$ and approximately $Re_{c_{\text{MAC}}} = 5.2 \times 10^6$ and from $\alpha = 2.0°$ to $7.0°$ at half degree intervals. The flow conditions and geometry parameters for the TTBW simulations are provided in Table 2. The HRLES coarse mesh simulation results presented were initialized as *cold-starts*, wherein the simulations for each angle-of-attack were initialized using a freestream condition. The simulations on the medium and fine mesh were initialized by interpolating the solution from the coarser grid (*e.g.* warm-start). Sensitivity tests were performed and no significant sensitivity to the initial condition was observed (not shown).



(a) $\alpha = 5.0°$ (HRLES) (b) $\alpha = 5.0°$ (URANS)

Fig. 5 Instantaneous visualization of the flow past the TTBW with iso-surfaces of Q-criterion (colored by u-velocity) for HRLES and URANS at $\alpha = 5.0°$. Iso-surfaces are deactivated on the fuselage.

We begin by examining the transonic flow characteristics and the behavior of the shielding function of the underlying HRLES turbulence modeling approach. Fig. 5 shows an instantaneous visualization of the flow past the TTBW with

iso-surfaces of Q-criterion (colored by u-velocity) for both HRLES and URANS at $\alpha = 5.0°$ on the fine mesh. On the main wing, the shock is visible on the upper surface with a significant spanwise variation of the shock position and vortices developing behind the shock for both HRLES and URANS. Moreover, for HRLES there appears to be no observable resolved turbulent content upstream on the shock indicating that the boundary-layer remains attached in this region and is modeled in RANS mode. Furthermore, It can be seen that for HRLES, the LES regions are capturing the resolved turbulent content where the boundary-layer is separating behind the shock.

Instantaneous contour maps on $y-$plane slices for Mach number (M) and shielding function (f_d) obtained with HRLES at $\alpha = 5.0°$ are presented in Fig. 6. The respective contour maps are clipped to show only regions where the flow is supersonic ($M > 1$) and is either in RANS mode or where hybrid model is switching from RANS to LES, namely, the *"grey-area"* ($f_d < 0.8$). The Mach number contour maps indicate that a *lambda shock* pattern[42] forms on the upper surface of the wing with; a normal shock developed away from the wall, an oblique shock forming at the wall upstream of the normal shock with the flow supersonic in region downstream of the shock, and the boundary-layer separating at the foot of the shock. As expected from DDES approaches, upstream of the shock close to the wall where the flow is attached on the wing, the boundary-layer is computed in RANS mode ($f_d = 0$) by the HRLES model. Conversely, downstream of the oblique shock, where the boundary-layer separation occurs, the flow is largely simulated in LES mode ($f_d = 1$). However, at the foot of the shock, where the flow separates and subsequently a shear layer is generated, the HRLES model persists in RANS mode for a portion of the chord downstream before developing into the *"grey-area"* and eventually LES mode. The behavior whereby the shear layer remains in RANS mode is part of the enhanced protection (EP) component of the HRLES model, namely, ZDES2020 mode 2 EP [17] approach and simulations (not shown here) confirm the same behavior does not occur with older iterations of DDES methods such as DDES[16]. The EP includes a *"second shielding function"*, f_{d2}, which employs a sensor, which in part, computes the normal derivative of eddy-viscosity to, as reported by Deck & Renard[17], detect the presence of wake layers of the attached boundary-layers and keep those regions in RANS mode.

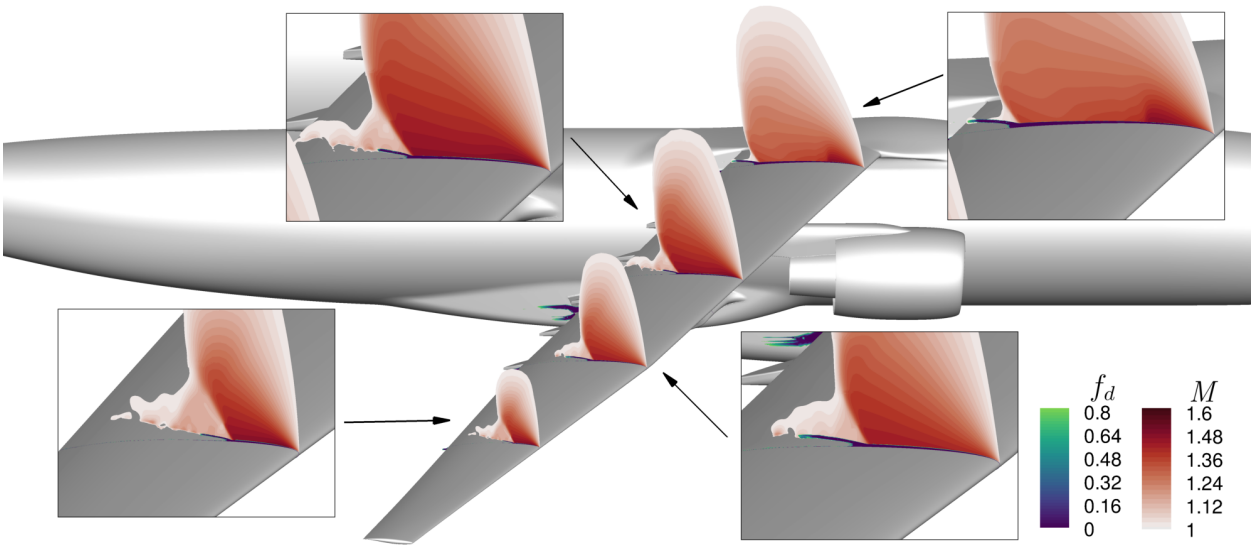
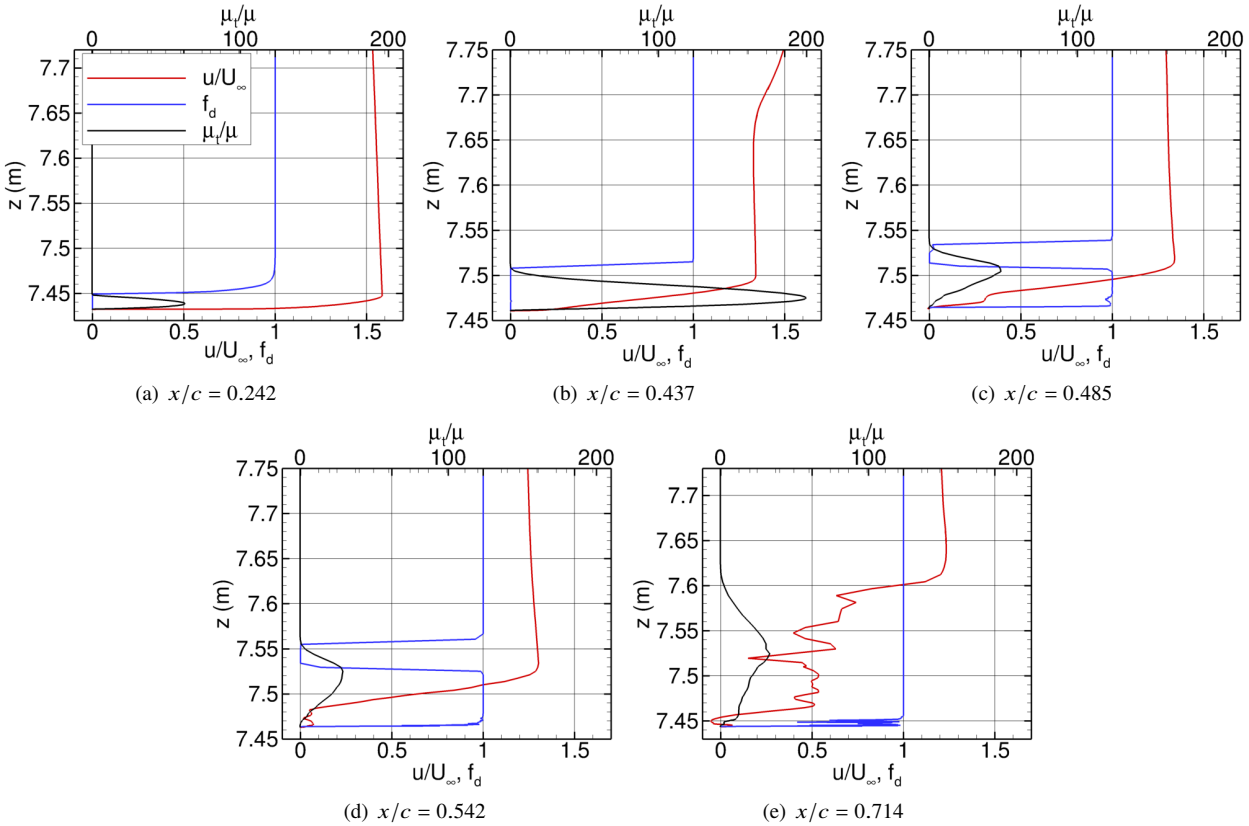


Fig. 6 Visualization of various $y-$plane slices of instantaneous Mach number (M) and shielding function (f_d) fields obtained with HRLES at $\alpha = 5.0°$. Only regions where $M > 1$ and $f_d < 0.8$ are shown.

A key question is whether the performance of the shielding function observed in Fig. 6 is both intended by the original authors and desirable for this type of transonic buffet flow. To understand this question further, instantaneous profiles of $u-$velocity (u/U_∞), shielding function (f_d) and eddy viscosity ratio (μ_t/μ) in the z-coordinate direction for five different chordwise locations at $\eta = 0.5541$ are presented in Fig. 7. Fig. 7(a) shows a profiles extracted at $x/c = 0.242$ which is upstream of the shock in the attacked flow region. At this location it can be seen that the boundary-layer is completely protected in RANS mode. At next profile at $x/c = 0.437$ in Fig. 7(b), which located just behind the shock, the boundary-layer is still shielded in RANS mode with a flattening in the gradient of the velocity profile seen. A more significant change is observed the next location in Fig. 7(c) where the profiles have been extracted in the region downstream of the shock that intersects with the off-wall RANS region. At this point the boundary-layer

has separated and the velocity profiles exhibits reverse flow close to the wall and there is an inflection in the velocity profile noticeable. The shielding function detects that the boundary-layer has separated and goes into LES mode. However, away from the wall, the *second shielding function* (f_{d2}) detects the change in slope of the eddy viscosity and returns the turbulence model to RANS mode to capture the upper region of the boundary-layer (*i.e.* the wake layer). The growth in the separation bubble can be seen in Fig. 7(d). In the last profile where shear layer has developed, the model is solving for the flow almost entirely in LES mode. The shielding function does not activate in RANS mode in the similar fashion as the prior two figures in the upper part of the profile where the drop in eddy viscosity is seen due to the *inhibition function* (f_r) that is also employed in the ZDES2020 mode 2 EP approach. The *inhibition function* is designed to prevent the second shielding function from activating in regions of the flow in RANS mode that have been erroneously determined to be wake layers when they are in fact in the early stages of a free shear layer. It appears from the profiles presented that the shielding function is functioning as designed although whether this is the desirable operation of the shielding function is much more challenging to answer. HRLES DDES approaches have struggled with buffet for problems such as NASA High-Speed Common Research Model (CRM-HS)[14] and the NACA0012[7] and have shown to predict the shock further upstream and a plateauing of the pressure behind the shock when compared to experiment. This paper will look to determine if these issues are still persistent for the TTBW with the ZDES2020 Mode 2 EP turbulence modeling approach.

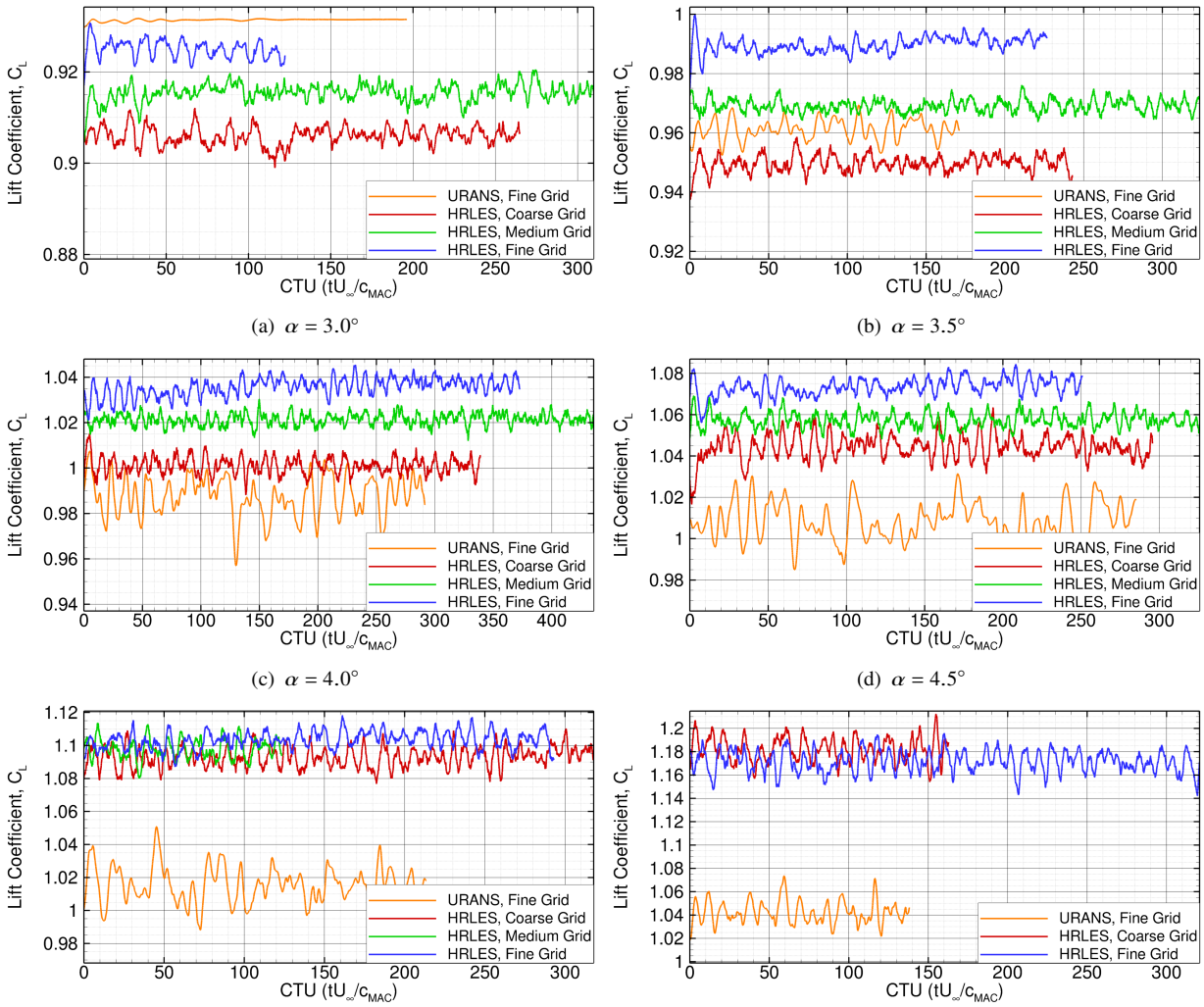


(a) $x/c = 0.242$ (b) $x/c = 0.437$ (c) $x/c = 0.485$

(d) $x/c = 0.542$ (e) $x/c = 0.714$

Fig. 7 Instantaneous profiles of u/U_∞, f_d and μ_t/μ at different chordwise locations at $\eta = 0.5541$.

Lastly, Fig. 8 shows the lift coefficient histories for some of the angles-of-attacks simulated. The initial transient part of the simulation from the start-up - generally 20-30 non-dimensional convective time units ($CTU = tU_{\text{ref}}/c_{\text{MAC}}$, where c_{MAC} is the mean aerodynamic chord)- has been discarded and only the time window which is utilized for averaging and computing PSD is shown in the plots. A large number of CTUs was needed when computing PSD to obtain adequate spectral resolution at the low frequency range where frequencies associated with buffet are located. The lift coefficient history at $\alpha = 2.5°$ (not shown in Fig. 8) was quasi-steady for HRLES - on coarse, medium and fine grids - and URANS. However, it can be seen in Fig. 8(a) at $\alpha = 3.0°$ that although URANS shows some small oscillations initially, the lift remains quasi-steady whereas all three HRLES meshes show some variation in the lift. At $\alpha = 3.5°$ all 4 solutions show



(a) $\alpha = 3.0°$ (b) $\alpha = 3.5°$

(c) $\alpha = 4.0°$ (d) $\alpha = 4.5°$

(e) $\alpha = 5.0°$ (f) $\alpha = 6.0°$

Fig. 8 Lift coefficient histories for various angles-of-attack for URANS and HRLES.

similar unsteadiness in the lift coefficient. At $\alpha = 3.5°$ and $\alpha = 4.5°$ there does not appear to be monotonic convergence although this is not expected due to the targeted refinement on the finest grid level. Improved convergence in the loads is seen for $\alpha > 4.5°$.

A. Time-Averaged Flow

Fig. 9 shows a comparison of the aerodynamic loads (C_L, C_D) and pitching-moment (C_{My}) coefficients for the α-sweep studied and obtained on the coarse, medium and fine grid resolutions investigated with HRLES. The URANS is simulated on the same fine grid as employed by the HRLES. The experiments utilized tripping strips at various chordwise locations on the main wing and strut. The HRLES simulations are compared to experimental data for various chordwise trip locations, namely: 5% x/c (run 492), 25% x/c (run 581) and 40% x/c (run 529). The error bars in the CFD curves show the minimum and maximum load/moment value obtained during the averaging window.

The predicted C_L and C_D with HRLES on all three grid levels shows a slight overprediction compared to the experimental results obtained with tripping at 5% x/c (run 492). Given that the SA RANS equations are assumed fully turbulent, it would be expected that our CFD should in principle align most closely with the tripping that is employed closest to the wing leading edge. This assumes that in the experiment that the tripping does cause a laminar-turbulent transition. All three grid levels with HRLES and URANS overpredict the experimental runs at the low angles-of-attack

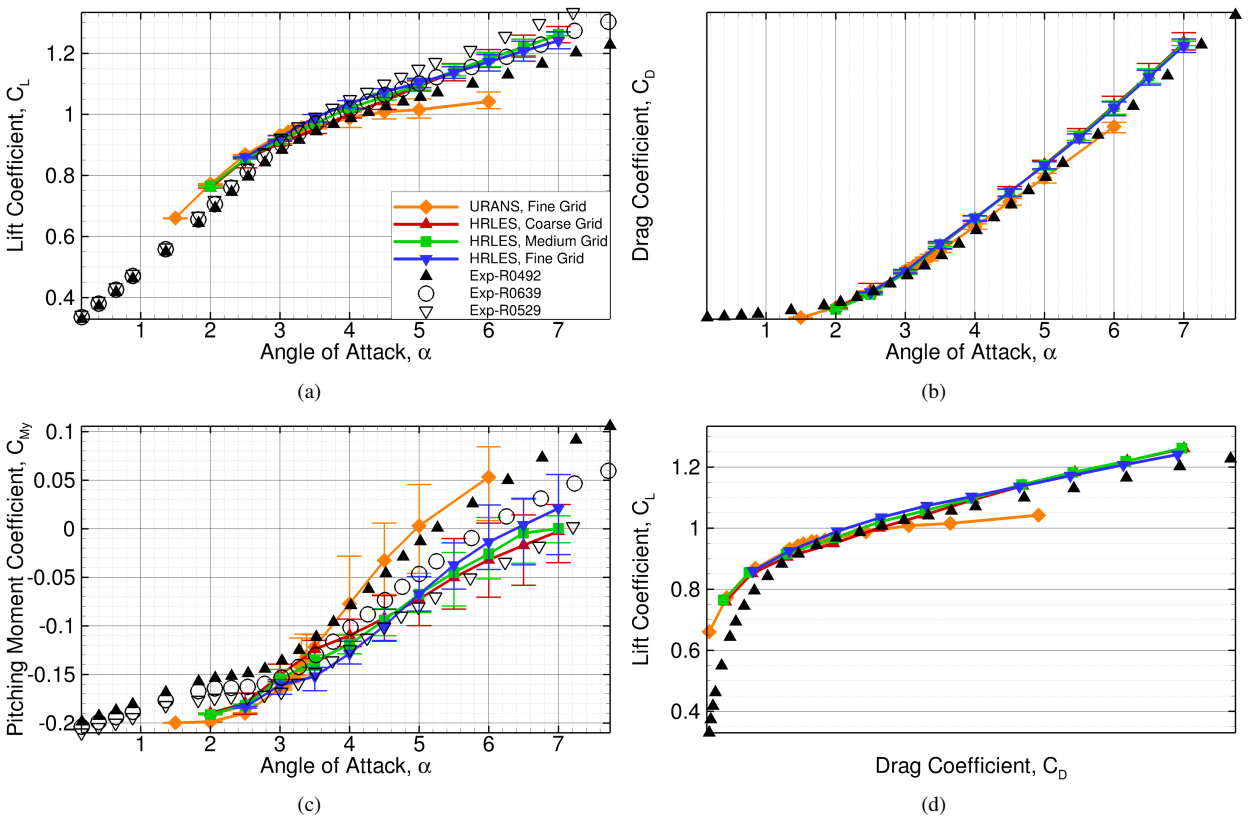


Fig. 9 Comparison of aerodynamic loads and moments with HRLES for various grid resolutions at $M = 0.8$. The error bars in the CFD curves show the minimum and maximum load/moment value obtained during the averaging window.

before the pitch break ($\alpha < 3^\circ$). After the pitch break, the predicted C_L with HRLES on the finest grid level initially shows better agreement with the 40% x/c tripped case whereas for $\alpha < 3^\circ$ better agreement is seen with 25% x/c tripped case. Overall, only minor variations in the predicted C_L and C_D are observed with increasing grid resolution. URANS shows better agreement with 5% x/c tripped case after the pitch break although at the higher angles shows a large underprediction. Similarly, URANS shows good agreement in pitching-moment after the pitch break but conversely shows an overprediction at the higher angles in Fig 9(c). A relatively larger sensitivity is seen for increasing grid resolution in the predicted C_{My} for HRLES. Furthermore, an underprediction in C_{My}, with respect to the 5% x/c tripped case, is seen although at some angles this underprediction is reduced with increasing mesh resolution. The C_L - C_D curve in Fig. 9(d) for HRLES on all mesh resolution shows reasonable agreement with the experiment with a slight overprediction at the higher drag values and the same larger overprediction in lift at the lower drag values that was noted above and seen in Fig 9(a). It is noteworthy that after the pitch-break there was a strong sensitivity to trip location in the experiment that is visible in the curves in Fig 9.

Next, the sensitivity to grid resolution is also analyzed for surface pressure coefficient at various stations along the wing and strut span. The predicted surface pressure from HRLES and URANS is compared to the experiment that was tripped at 5% x/c.

Firstly, we examine one of the lower angles-of-attack to determine the cause of the overprediction in lift seen in Fig. 9(a). This flow condition in the tunnel is near the aeroelastic design point of the model which would provide the ideal 1-g wing shape, which is used in the CFD modeling. Fig. 10 shows the surface pressure coefficient predicted with HRLES/URANS and compared with the experiment at various inboard, midboard and outboard stations along the main wing. All six stations show that the CFD overpredicts the shock location on the upper surface over the main wing. There is no noticeable improvement in the shock location with higher grid resolution or utilizing URANS. This behavior has been observed in prior studies with the TTBW[43, 44] and appears to be related to the SA turbulence model with

improved predictions seen for RANS when employing the $k-\omega$ shear stress transport (SST) turbulence model. This overprediction in C_p is the likely the cause of the overprediction in lift seen at the lower angles-of-attack. At $\eta = 0.0716$ in Fig. 10(a), which is very close to the wing root, the overprediction persists across the angle-of-attack sweep, therefore at this station the overprediction may be due to the wind tunnel floor effects not being captured in the free air CFD simulations. Although there is significant overprediction in the shock at all the stations, upstream and downstream of the shock the surface pressure shows good agreement with the experiment.

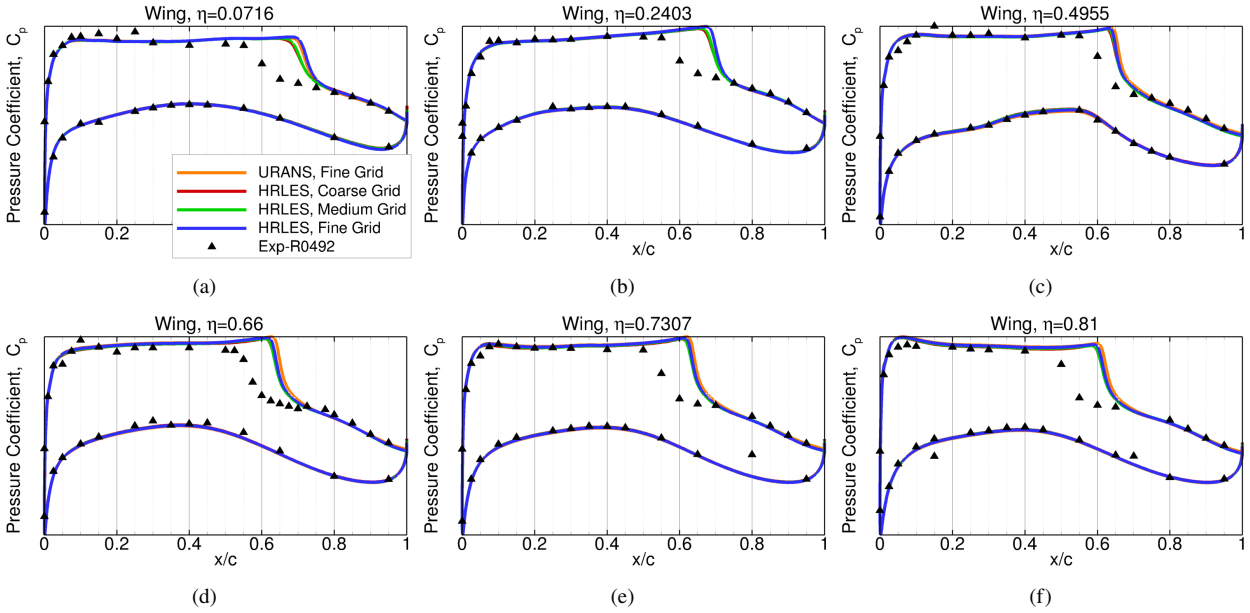


Fig. 10 Variations in surface pressure coefficient (C_p) slices along the wingspan of the TTBW with the HRLES modeling approach for various grid resolutions at $M = 0.8$ and $\alpha = 2.5°$.

There is an improvement in the prediction of the chordwise shock location with HRLES and URANS when moving to $\alpha = 3.0°$ as shown in Fig. 11. At the outboard station $\eta = 0.81$ both HRLES and URANS show good agreement with the experimental surface pressure. However, at the midboard stations ($\eta = 0.4955$ and $\eta = 0.5541$), HRLES on the coarse grid level underpredicts (more upstream) the shock location, features a plateau of the surface pressure immediately behind the shock and then predicts a lower pressure level downstream of the shock when compared to the experiment. With increasing grid resolution, the HRLES predicts a shock further downstream and shows a trend of increasing pressure downstream extending to the trailing edge of the suction side of the wing which results in better agreement with the experiment. URANS computed on the fine grid level shows excellent agreement at all three spanwise stations presented. In Fig. 11(b) at $\eta = 0.5541$ it can be seen that a shock forms on the pressure side of the wing between 0.45-0.5 x/c which corresponds well to the experiment. This station is very close to the wing-strut juncture, and a the shock develops in the narrow channel between the wing and strut. The shock was also observed in the CFD and experiment at lower angles studied ($\alpha = 2$ and 2.5).

At $\alpha = 4.0°$ in Fig. 12 a similar trend is seen for surface pressure with HRLES for increasing mesh resolution. At the outboard stations $\eta = 0.81$ and $\eta = 0.8826$, the HRLES solution on the fine grid level predicts a shock slightly upstream of the experiment and a plateau in surface pressure which extends approximately 20% of the chord is also observed similar to the behavior seen at the midboard stations at the $\alpha = 3.0°$ case. It can be seen that there is very good agreement in the predicted shock location at the midboard stations with HRLES on the fine grid compared to the experiment. URANS shows good agreement with the experiment at most of the stations although we see the shock retreat upstream of the experiment at $\eta = 0.66$. Improvements are also seen on the strut with HRLES and URANS (both fine grid level) showing closer agreement with the experiment on the upper surface of the strut at $\eta = 0.3272$ in Fig. 12(f).

Finally, Figs. 13 and 14 show the surface pressure computed with HRLES and URANS are $\alpha = 5.0°$ and $\alpha = 6.0°$, respectively. Relatively less sensitivity is observed in the predicted shock location with HRLES when varying the grid resolution when compared to the lower angles-of-attack. Good agreement is observed for HRLES in the prediction of

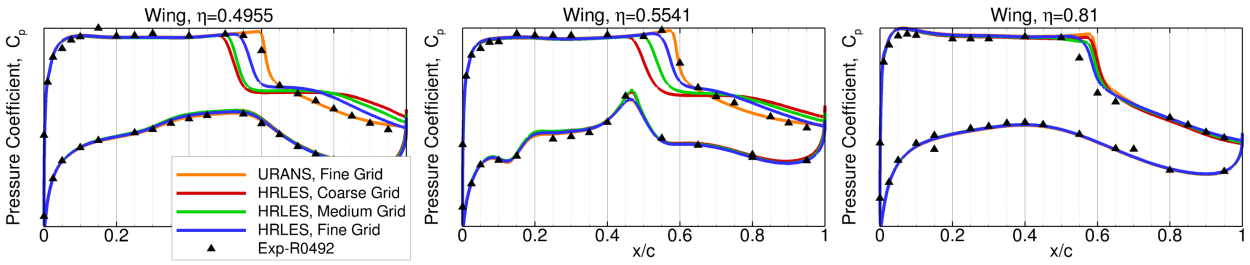


Fig. 11 Variations in surface pressure coefficient (C_p) slices along the wingspan of the TTBW with the HRLES modeling approach for various grid resolutions at $M = 0.8$ and $\alpha = 3.0°$.

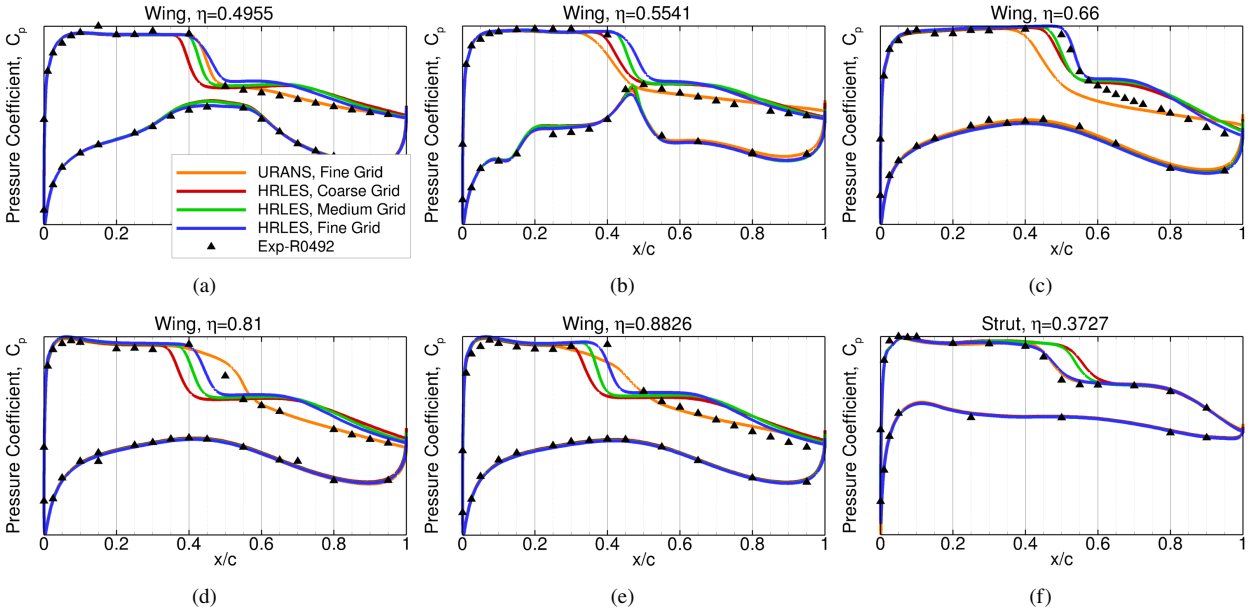


Fig. 12 Variations in surface pressure coefficient (C_p) slices along the wingspan of the TTBW with the HRLES modeling approach for various grid resolutions at $M = 0.8$ and $\alpha = 4.0°$.

the shock location at both the higher angles-of-attack compared to the experimental data although there still persists an underprediction in the pressure level downstream of the shock. The pressure level appears to recover and show reasonable agreement with the experiment for $x/c > 0.8$. Furthermore, it can be seen that HRLES gives a superior prediction of the overall surface pressure when compared to URANS which in particular tends to predict the shock location significantly upstream of the experiment.

The surface pressure curves obtained from HRLES and the wind tunnel experiment that are shown in Fig. 12 and 14 for $\alpha = 4.0°$ and $\alpha = 6.0°$ respectively are also visualized and compared in Fig. 15 as surface pressure coefficient contour plots of the upper surface on the main wing. Reasonable qualitative agreement can be seen in the shock locations for both angles. The delay in the pressure rise downstream of the shock with HRLES is noticeable at $\alpha = 4.0°$ case.

It has been shown that on the coarse grid level that the HRLES method has shown the same issue with similar DDES approaches that has been seen by other authors for transonic flow cases[7, 14]. Namely, the shock is predicted further upstream compared to the wind tunnel experiment and a large separation region develops behind the shock which results in the plateauing of the pressure and an underprediction is the pressure from the shock to the trailing edge of the wing. However, with increasing grid resolution there is a better agreement in the shock position and the pressure starts showing a similar trend with the experiment downstream of the shock and beginning at the trailing edge. The overall trend appears to indicate that with continuing refinement of the mesh that better agreement will be

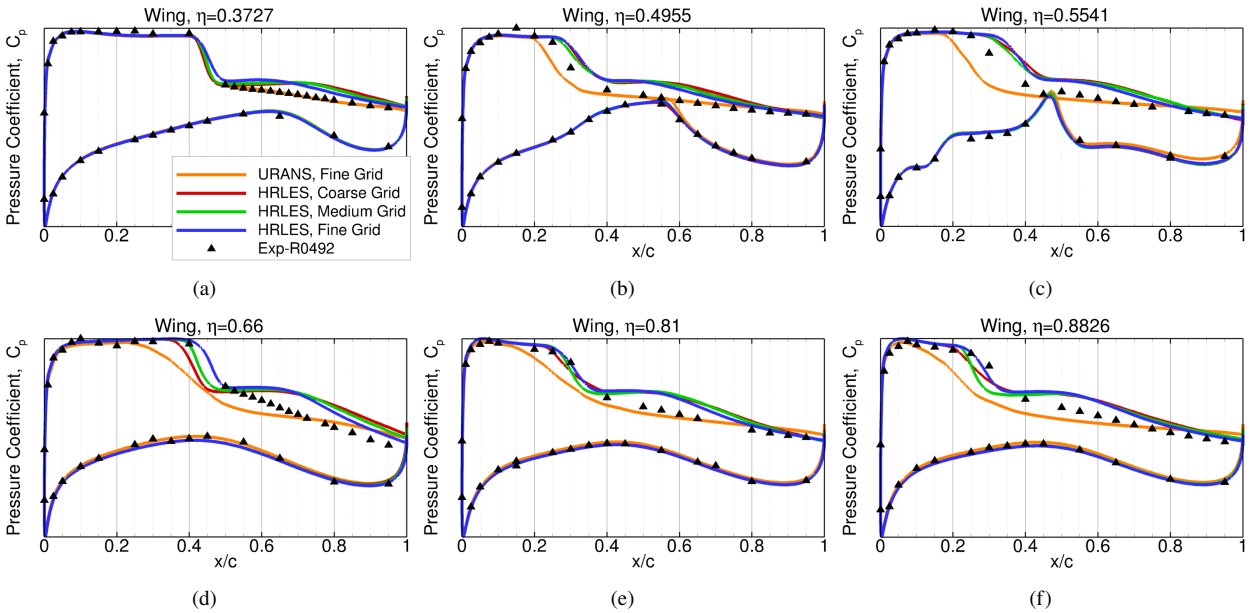


Fig. 13 Variations in surface pressure coefficient (C_p) slices along the wingspan of the TTBW with the HRLES modeling approach for various grid resolutions at $M = 0.8$ and $\alpha = 5.0°$.

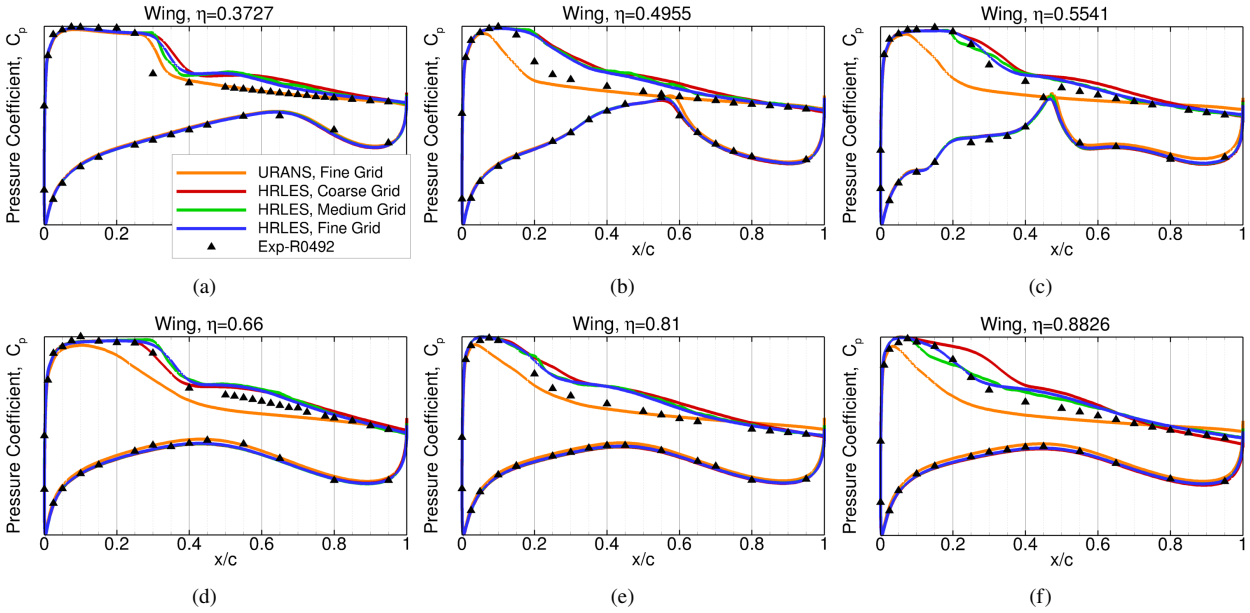
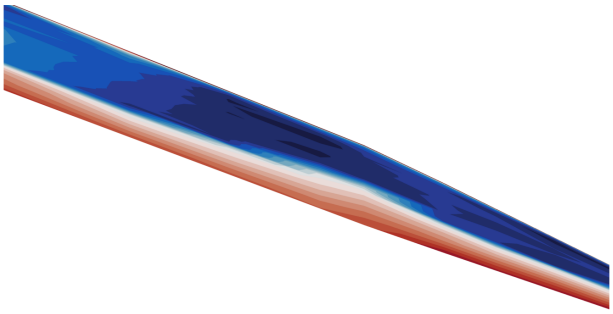


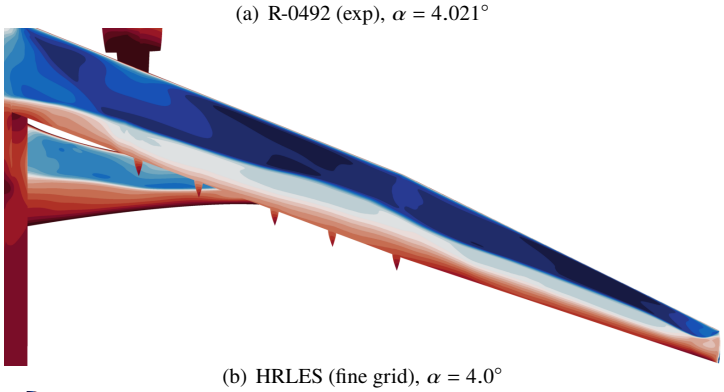
Fig. 14 Variations in surface pressure coefficient (C_p) slices along the wingspan of the TTBW with the HRLES modeling approach for various grid resolutions at $M = 0.8$ and $\alpha = 6.0°$.

reached (remains to be seen if this holds for further grid refinement). This is in contrast to DES and DDES whereby with increasing grid refinement, at a certain point, inferior predictions in the separated flow region were obtained[45]. Generally, HRLES shows better agreement at the higher angles while URANS performs well at the lower angles and shows reduced agreement at the higher angles-of-attack.

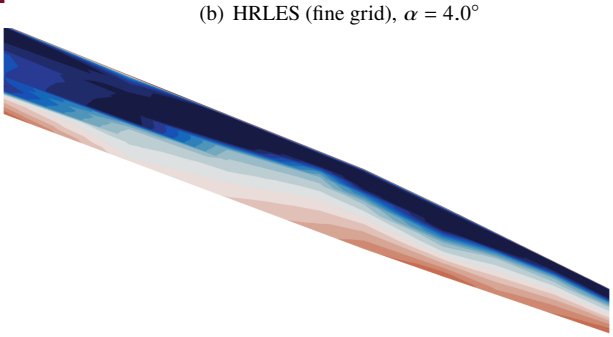
Transonic buffet is a particularly challenging problem for DDES approaches (including ZDES2020 mode 2 EP) due to unsteady nature of the shock which requires that the hybrid model is, in regions in the vicinity of the shock, switching



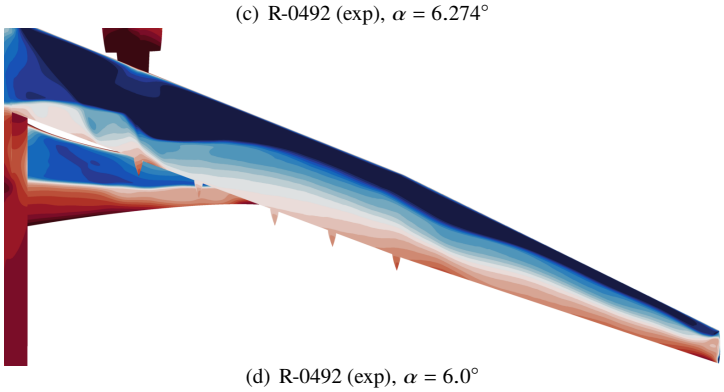
(a) R-0492 (exp), α = 4.021°



(b) HRLES (fine grid), α = 4.0°



(c) R-0492 (exp), α = 6.274°



(d) R-0492 (exp), α = 6.0°

Fig. 15 Comparison of the time averaged surface pressure coefficient (C_p) on wingspan of the TTBW obtained with HRLES (fine grid) and the experiment at $\alpha = 4.0°$ and $\alpha = 6.0°$. Surface pressure contour for the experiment is generated from the values obtained from the pressure taps in Fig. 4(a).

between RANS and LES mode as the shock moves back and forth over the wing. There needs to be sufficient turbulent fluctuations when going into LES mode otherwise the sudden loss of modeled-stress which is not compensated for by

any resolved content (resolved Reynolds stress) leads to the well known phenomenon called modeled stress depletion (MSD). This could be a possible cause of the excessive separation seen behind the shock.

Finally, a comparison of the time-averaged x-component of the skin friction coefficient (c_{f_x}) for HRLES and URANS on the fine grid level at $\alpha = 2.5°, 3.0°, 3.5°$ and $4.5°$ are shown in Fig. 16. The contour map has been clipped to shown only $(c_{f_x}) > 0$ to show regions on separated flow. Both URANS and HRLES show a small separated region forming at $\alpha = 2.5°$ in the mid-span region right behind the shock. Similar flow topology is seen at $\alpha = 3.0$ with the midboard region largely separated and the separation also extends inboard to the nacelle pylon. The most significant difference is at $\alpha = 3.5$ and $4.5°$ where the flow is mostly attached on the outboard wing with URANS and HRLES shows significant flow separation. In the latter case, the attached flow on the outboard corresponds to the improvement seen in the pressure curves at the region that was shown above.

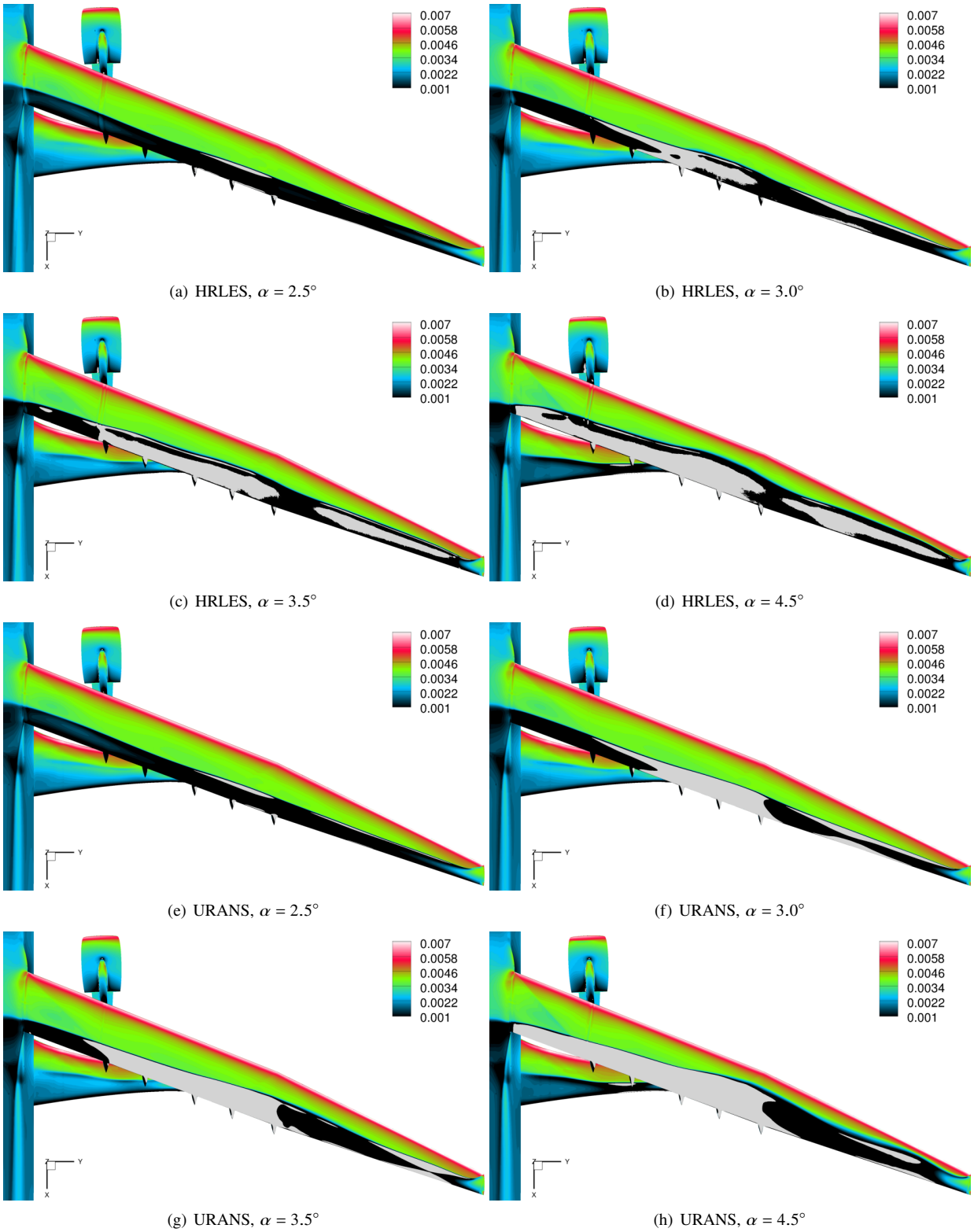
B. Unsteady Pressures

Fig. 17 shows a comparison of the instantaneous surface pressure coefficient across the angle-of-attack sweep computed with HRLES and URANS on the fine grid level. At $\alpha = 2.5°$ very similar flow topologies are obtained with the HRLES and URANS with a shock running approximately parallel to the trailing edge of the wing. The flow appears relatively steady which is also confirmed by examining in the aerodynamic load histories. Next, at $\alpha = 3.0°$ the HRLES solution shows some flow unsteadiness and oscillations in the shock at the mid-span region of the main wing. Furthermore, the shock has moved slightly upstream which is also visible in the URANS solution. The flow unsteadiness and shock oscillations has extended to inboard and outboard regions of the main wing at $\alpha = 3.5°$ and $\alpha = 4.0°$ for both HRLES and URANS. Moreover, for the $\alpha = 6.0°$ case both solution approaches yield a flow topology where the shock has moved significantly towards the leading edge across the span of the wing and flow unsteadiness has also developed on upper surface of the strut.

Figs 4(b) and 4(c) shows the positions on the main wing and strut where unsteady pressures were recorded in the simulations. Subsequently, power spectral densities (PSD) and root mean square (RMS) were computed from unsteady pressures. PSD spectra can be utilized to determine both the frequency of the buffet instability mechanism and the buffet onset or boundary based on varying flow conditions such as Mach number or angle-of-attack. To allow for comparison between the full scale CFD TTBW model and the scale model from the experiment, PSD and RMS values obtained from the experiment were scaled by multiplying with the ratio of the dynamic pressures (q), whereby: $(q_{\text{CFD}}/q_{\text{exp}})^2$ - PSD scale, and $q_{\text{CFD}}/q_{\text{exp}}$ - RMS scale. For the PSD computation, a bin frequency of 1.5 Hz was selected with Hann windowing and 50% overlap. The PSD spectra is plotted against nondimensional frequency Strouhal number ($St = fc_{MAC}/U_\infty$) and a frequency scaling is applied to the experimental data to compare with the CFD. The CFD simulations were generally run for between 200-300 CTUs (see Fig. 8) and are compared to experimental data which is sampled over a similar time interval (reduced sample) and a full sample from the experiment. Frequency values are not included due to data restrictions but a grey shaded region is included in the plots which indicates the frequency band which is a region of interest for transonic buffet.

Figs. 18 - 21 shows comparisons between PSDs obtained from the two simulation approaches (HRLES and URANS) and experiment at midboard and outboard locations at different angles over the alpha sweep. Run 500 was selected, from the limited set of runs from the experiment where Kulites were utilized for a full angle-of-attack sweep and a pitch-pause method was employed, as the comparison dataset. A few of the Kulites were not functioning during Run 500, so we also include data from an earlier Run 144 where the Kulites were still working. Run 500 and 144 employed tripping at 40% x/c and 5% x/c chordwise locations respectively on the main wing. Figs. 18 and 20 show the development of the PSD spectra at three midboard locations ($\eta = 0.5, 0.6$ and 0.65) on the main wing with increasing angle-of-attack. The purple bands in Fig. 18(a) - 18(b) indicate frequency bands where known tones are present that are inherent to the wind tunnel and have been identified from running the tunnel empty without a test article[46]. It can be seen that the highest frequency tunnel tone is persistent at a significant PSD level at most of the angles-of-attack shown and would not be captured by the CFD in the free air configuration.

At $\alpha = 3.5°$ HRLES predict higher levels of PSD than the experiment across almost the entire frequency range at the midspan (Fig. 18) and outboard (Fig. 20) probes. Moreover, The peak for HRLES is predicted towards the lower end of the frequency spectrum in the grey shaded region. The experiment also shows are sharp rise in PSD level at $\eta = 0.6, x/c = 0.8$ but with a lower peak when compared to HRLES. The PSD predicted with URANS shows reasonable agreement with HRLES at some locations (*e.g.* $\eta = 0.6, x/c = 0.8$) but diverges and predicts different behavior at other locations. When moving to higher frequencies beyond the grey buffet region the URANS PSD level decays much faster than both HRLES and the experiment due to the lack of resolved turbulent content. At $\alpha = 4.0°$, better agreement is



(a) HRLES, $\alpha = 2.5°$

(b) HRLES, $\alpha = 3.0°$

(c) HRLES, $\alpha = 3.5°$

(d) HRLES, $\alpha = 4.5°$

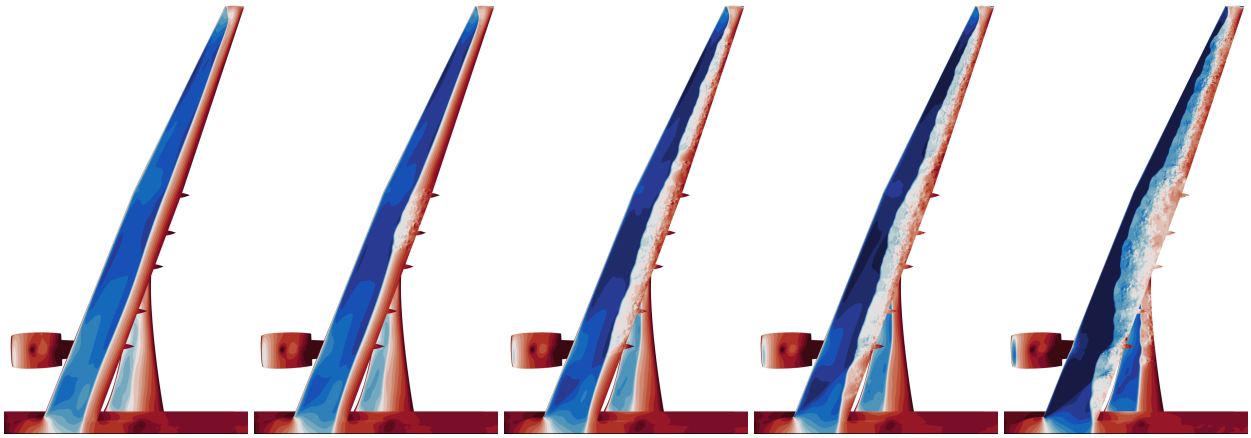
(e) URANS, $\alpha = 2.5°$

(f) URANS, $\alpha = 3.0°$

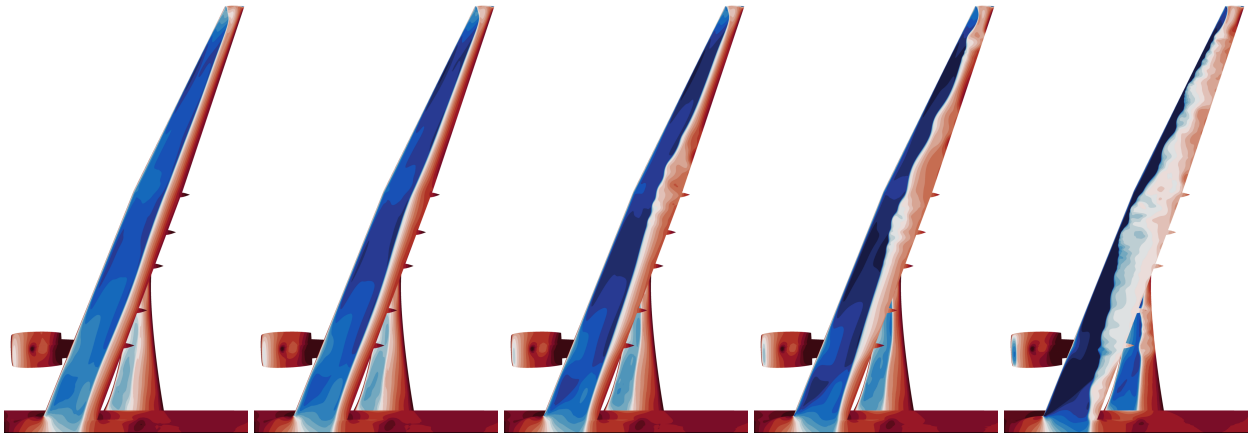
(g) URANS, $\alpha = 3.5°$

(h) URANS, $\alpha = 4.5°$

Fig. 16 Comparison of time-averaged skin friction coefficient (c_{f_x}) at various angles of attack obtained with a HRLES and URANS on the fine grid level.



(a) HRLES, $\alpha = 2.5°$ (b) HRLES, $\alpha = 3.0°$ (c) HRLES, $\alpha = 3.5°$ (d) HRLES, $\alpha = 4.0°$ (e) HRLES, $\alpha = 6.0°$

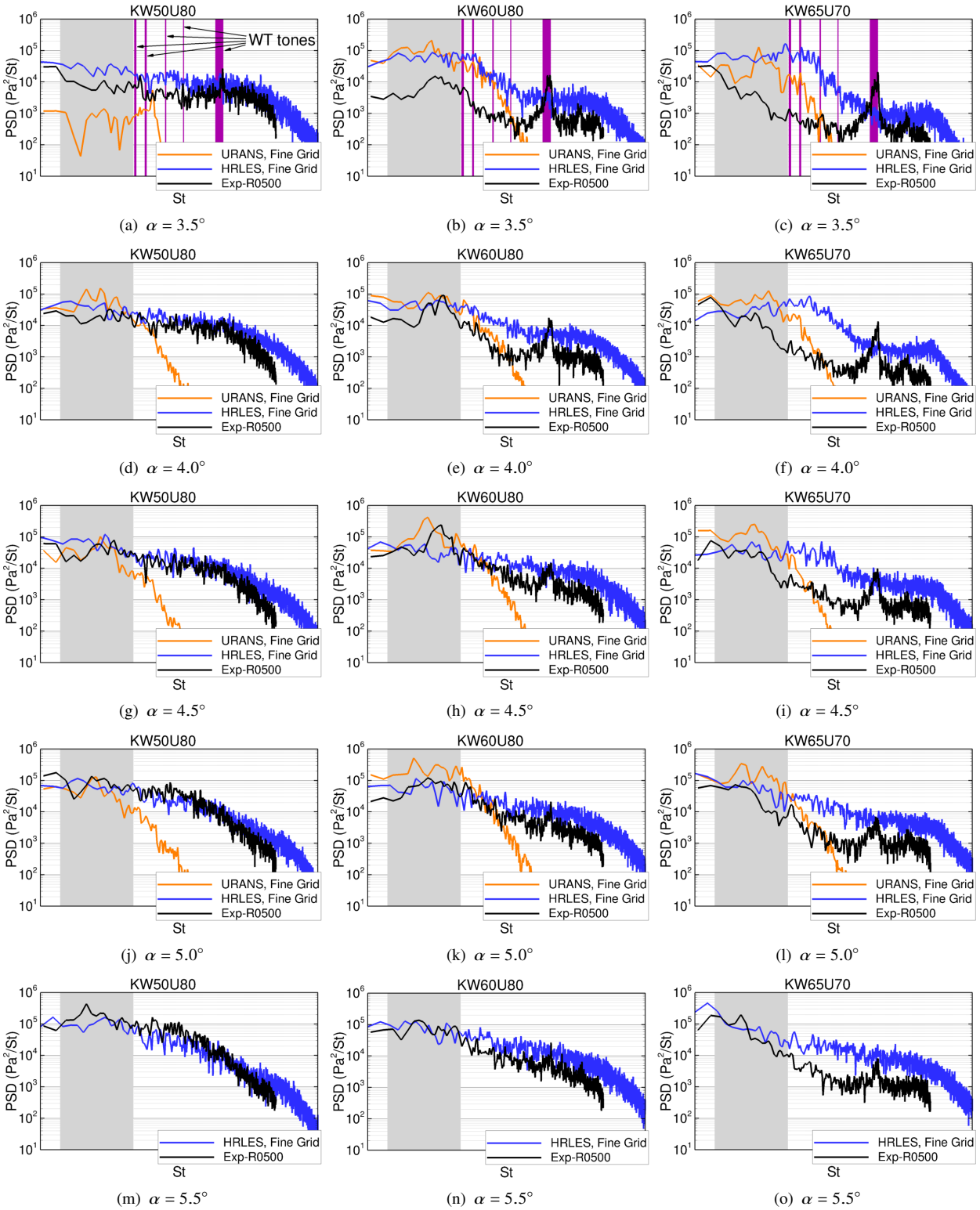


(f) URANS, $\alpha = 2.5°$ (g) URANS, $\alpha = 3.0°$ (h) URANS, $\alpha = 3.5°$ (i) URANS, $\alpha = 4.0°$ (j) URANS, $\alpha = 6.0°$

Fig. 17 Comparison of instantaneous surface pressure coefficient (C_p) at various angles-of-attack obtained with HRLES (top row) and URANS (bottom row). Both solutions were computed on the fine grid level. For the contour map, blue indicates lower pressure and red is higher pressure.

seen between simulations and the experiment in terms of the predicted peak in PSD level and the overall broadband spectra at $\eta = 0.5, x/c = 0.8$ and $\eta = 0.6, x/c = 0.8$. However, HRLES does predict a higher PSD level at the higher frequency range compared to the experiment. Both HRLES and URANS show overpredicitons in PSD level at the more outboard locations. Qualitatively, it appeared from the instantaneous unsteady surface pressure coefficient fields in Fig. 17 that the unsteadiness in the shock (buffet) originated in the midspan region. The experimental data shows an almost order of magnitude rise in the peak PSD at frequencies relevant to buffet between $\alpha = 3.5°$ and $\alpha = 4.0°$ at $\eta = 0.6, x/c = 0.8$. The overprediction in the PSD level at $\alpha = 3.5°$ may indicate that both URANS and HRLES predict an earlier onset of the development of buffet or at least the instability mechanisms that drive buffet. At the next angle shown, $\alpha = 4.5°$, better agreement in the PSD for frequencies associated with buffet is also seen at the outboard locations $\eta = 0.72, x/c = 0.8$ (Fig. 19(g)), $\eta = 0.8, x/c = 0.8$ (Fig. 19(h)) and $\eta = 0.89, x/c = 0.8$ (Fig. 19(i)) between the experiment and HRLES. However, there is a pronounced peak at $\eta = 0.6, x/c = 0.8$ in the experimental data which is located towards the higher frequency end of the grey shaded region that does not appear to be captured by HRLES. URANS does predict a sharp peak, although at a slightly lower frequency, but also overpredicts the peak PSD level at most of the other locations shown. At subsequently higher angles-of-attack, $\alpha = 5.0°$ - $\alpha = 6.5°$, HRLES shows improved prediction of the peak PSD level and the overall spectra when compared to the experiment. Furthermore, the overprediction in the PSD level at the higher frequencies with HRLES which was seen at lower angles is no longer present at the higher angles. URANS continues to show varying levels of agreement across wingspan at $\alpha = 5.0°$ and

$\alpha = 6.0°$ which is consistent with the trend of higher pressure predicted downstream of the shock that was seen in the time-averaged surface pressure coefficient curves presented in Fig. 13 and 14.



(a) $\alpha = 3.5°$ (b) $\alpha = 3.5°$ (c) $\alpha = 3.5°$

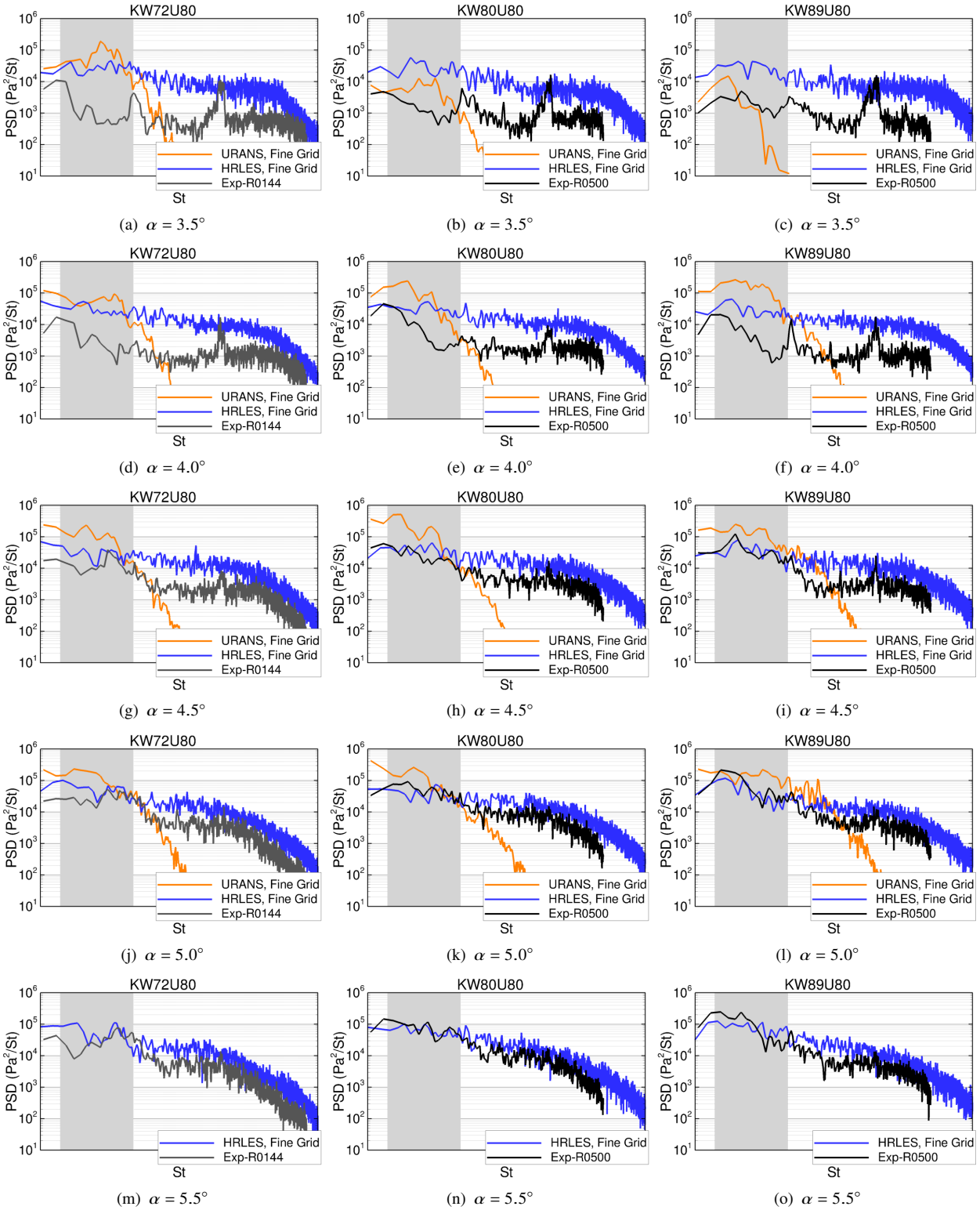
(d) $\alpha = 4.0°$ (e) $\alpha = 4.0°$ (f) $\alpha = 4.0°$

(g) $\alpha = 4.5°$ (h) $\alpha = 4.5°$ (i) $\alpha = 4.5°$

(j) $\alpha = 5.0°$ (k) $\alpha = 5.0°$ (l) $\alpha = 5.0°$

(m) $\alpha = 5.5°$ (n) $\alpha = 5.5°$ (o) $\alpha = 5.5°$

Fig. 18 PSD spectra obtained at midboard locations of the main wing of the TTBW at various angles-of-attack.



(a) $\alpha = 3.5°$ (b) $\alpha = 3.5°$ (c) $\alpha = 3.5°$

(d) $\alpha = 4.0°$ (e) $\alpha = 4.0°$ (f) $\alpha = 4.0°$

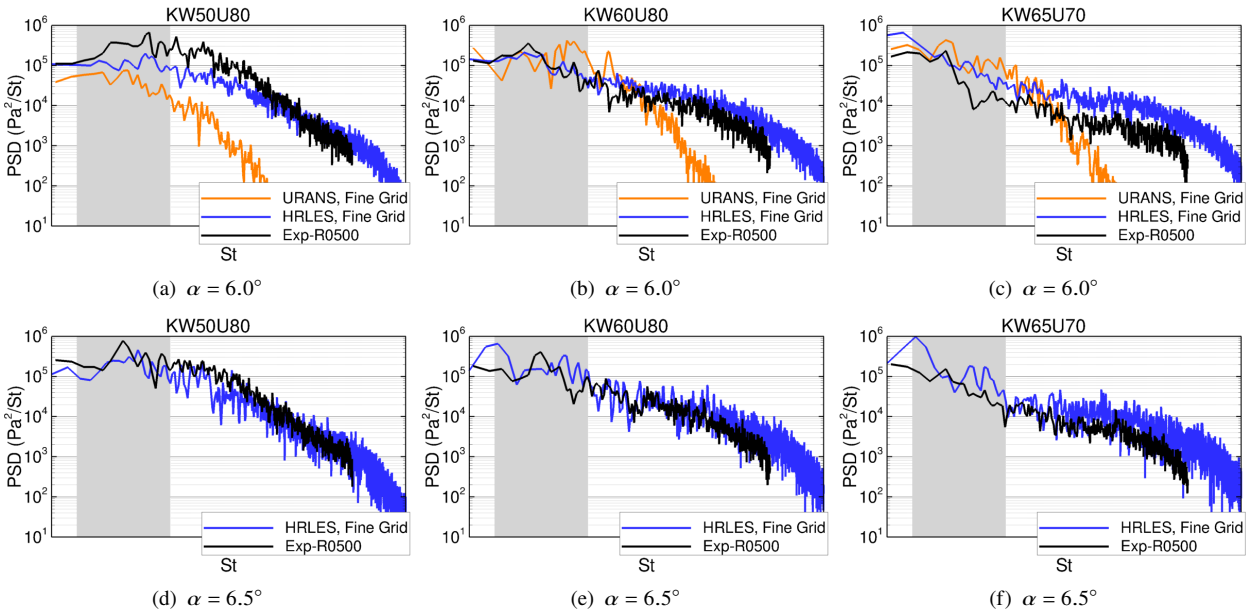
(g) $\alpha = 4.5°$ (h) $\alpha = 4.5°$ (i) $\alpha = 4.5°$

(j) $\alpha = 5.0°$ (k) $\alpha = 5.0°$ (l) $\alpha = 5.0°$

(m) $\alpha = 5.5°$ (n) $\alpha = 5.5°$ (o) $\alpha = 5.5°$

Fig. 19 PSD spectra obtained at outboard locations of the main wing of the TTBW at various angles- of-attack.

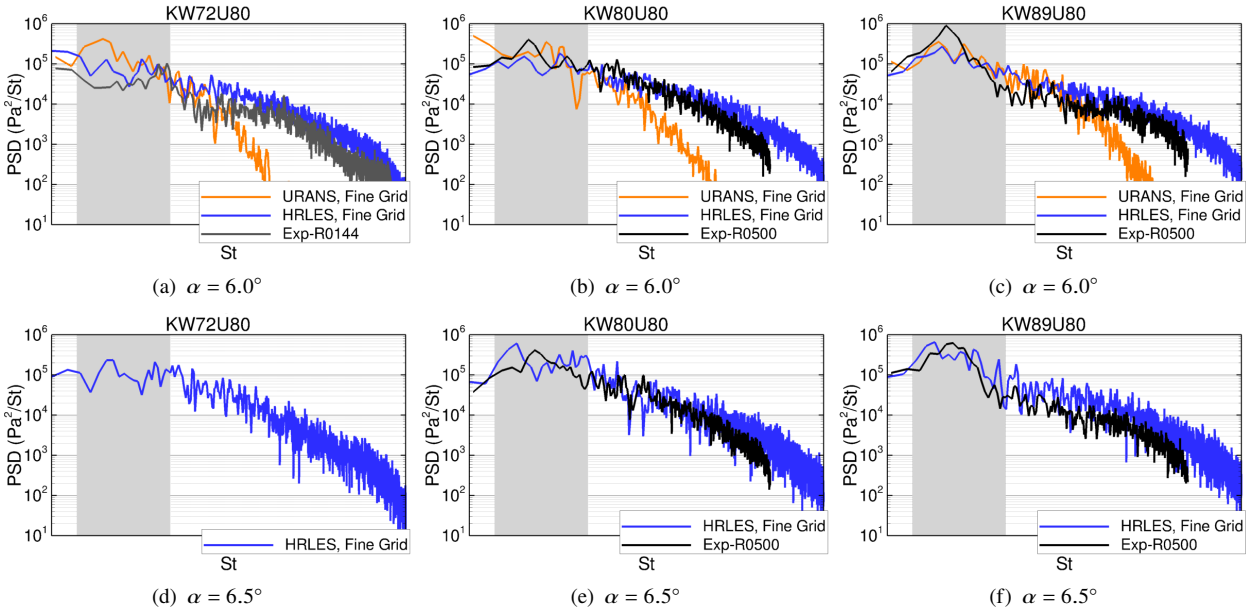
Fig. 22 and 24 visualizes the PSD curves as a contour map with angle-of-attack plotted against Strouhal number. These plots can be useful in determining buffet onset or the buffet boundary with respect to varying angle-of-attack.



(a) $\alpha = 6.0°$ (b) $\alpha = 6.0°$ (c) $\alpha = 6.0°$

(d) $\alpha = 6.5°$ (e) $\alpha = 6.5°$ (f) $\alpha = 6.5°$

Fig. 20 PSD spectra obtained at midboard locations of the main wing of the TTBW at $\alpha = 6.0°$ and $\alpha = 6.5°$.



(a) $\alpha = 6.0°$ (b) $\alpha = 6.0°$ (c) $\alpha = 6.0°$

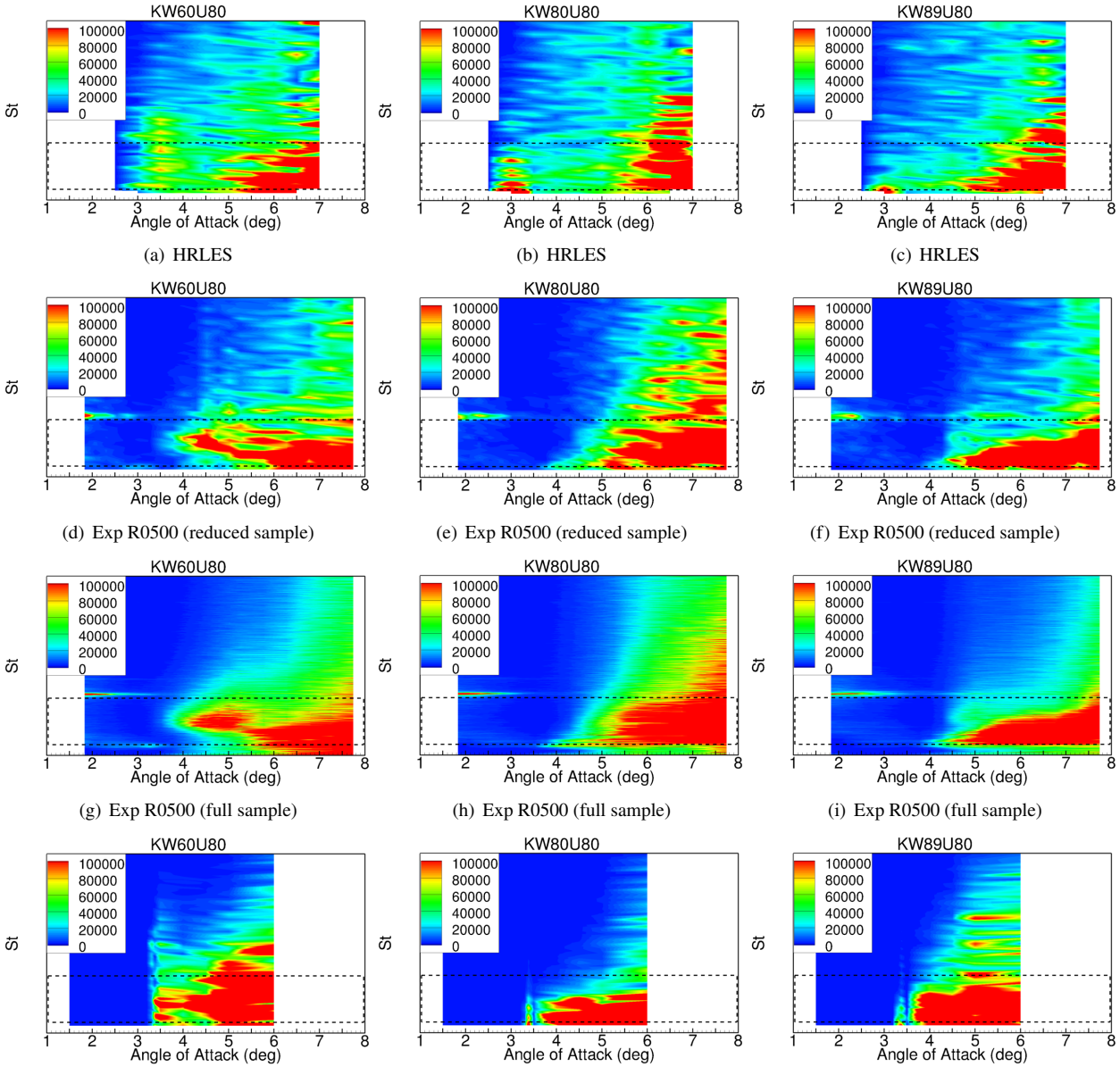
(d) $\alpha = 6.5°$ (e) $\alpha = 6.5°$ (f) $\alpha = 6.5°$

Fig. 21 PSD spectra obtained at outboard locations of the main wing of the TTBW at $\alpha = 6.0°$ and $\alpha = 6.5°$.

The black dashed line box represents same region as the grey shaded region shown in the PSD spectra curves. At the mid-span location, $\eta = 0.6, x/c = 0.8$, a band of excited frequencies where the PSD exhibits a sharp rise is visible in both HRLES and URANS at approximately $\alpha = 3.5°$. The in-tunnel experiment appears to show a rise in PSD between $\alpha = 3.5°$ and $\alpha = 4.0°$. Furthermore, the experiment shows the band of excited frequencies shift to a lower set of frequencies at between $\alpha = 5.0°$ and $\alpha = 5.5°$. In the frequency range associated with buffet (black dashed box), HRLES shows fair agreement with experimental data for $\alpha \geq 5.0°$. At the lower angles-of-attack it appears that HRLES predicts a slightly earlier onset of buffet. Similarly, URANS also appears to predict an earlier onset of buffet and show overpredictions in the PSD at the low frequency range. Conversely, URANS shows better agreement with the

experiment for p_{RMS} as shown in Fig. 23. HRLES shows an overprediction in the p_{RMS} which is consistent with the excessive separation observed in the C_p curves.

The lowest frequency that can be resolved and the resolution at the lower frequencies is a direct function of the length the time sample. As a result of the low frequency range that buffet occurs at, the CFD simulations need to be run out for hundreds of CTUs. Hence, to reduce the noise and increase the resolution in the frequency content of the CFD could be achieved by running out the simulations out even longer.



(a) HRLES (b) HRLES (c) HRLES

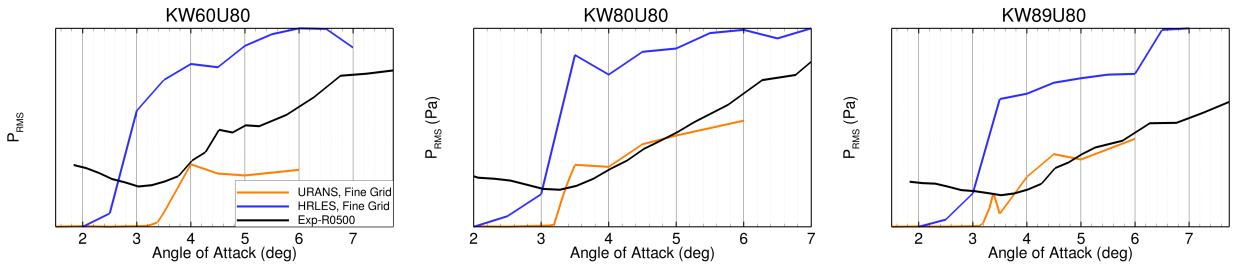
(d) Exp R0500 (reduced sample) (e) Exp R0500 (reduced sample) (f) Exp R0500 (reduced sample)

(g) Exp R0500 (full sample) (h) Exp R0500 (full sample) (i) Exp R0500 (full sample)

(j) URANS (k) URANS (l) URANS

Fig. 22 Contour plots showing the PSD spectra obtained from HRLES, URANS and the wind tunnel experiment for varying angle-of-attack at three locations on the main wing: $\eta = 0.6, x/c = 0.8$, $\eta = 0.8, x/c = 0.8$ and $\eta = 0.89, x/c = 0.8$. PSD computed with both the full sample and a reduced sample from the experiment is shown. The black dashed line box represents the same region as the grey shaded region shown in the PSD spectra curves.

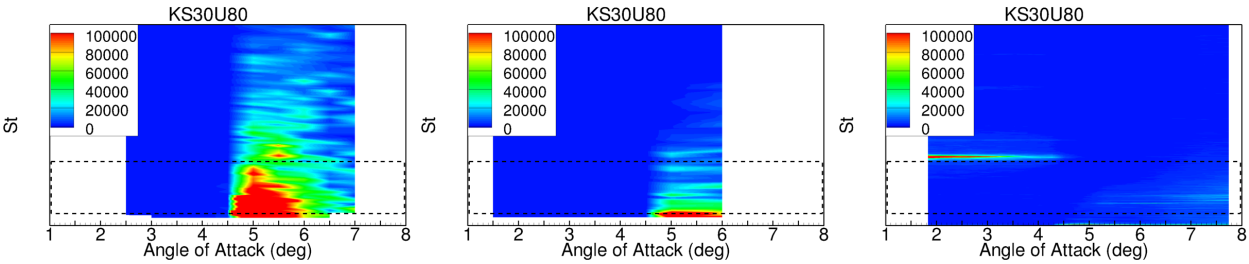
Finally, Fig. 24 shows PSD spectra contour plots at a location on the upper surface of the main strut $\eta = 0.3, x/c = 0.8$. The wind tunnel PSD does not appear to show any evidence of buffet in the wing-strut channel. HRLES and to a lesser



(a) (b) (c)

Fig. 23 p_{RMS} curves obtained from HRLES, URANS and the wind tunnel experiment for varying angle-of-attack at a location on the upper surface of the strut - $\eta = 0.3, x/c = 0.8$.

extent URANS, show a band of excited frequencies which may indicate that buffet is predicted between $\alpha = 4.5°$ and $\alpha = 6.0°$. It remains to be seen if this is a modeling error or a difference between the free air and in-tunnel configuration.



(a) HRLES (b) URANS (c) Exp R0500 (full sample)

Fig. 24 Contour plots showing the PSD spectra obtained from HRLES, URANS and the wind tunnel experiment for varying angle-of-attack at a location on the upper surface of the strut - $\eta = 0.3, x/c = 0.8$. The black dashed line box represents the same region as the grey shaded region shown in the PSD spectra curves.

V. Conclusions

An investigation of the capability of a scale resolving HRLES turbulence modeling approach to predict transonic buffet for the TTBW in a free air configuration has been presented. The flow past the TTBW was simulated with HRLES on three different grid resolutions and the results compared to URANS simulations and experiments conducted at the NASA Ames 11-by 11-Foot Transonic Wind Tunnel.

The key findings of the paper can be summarized as follows:

1) The aerodynamic loads predicted by HRLES show reasonable agreement with the wind-tunnel experiment with a slight overprediction of the lift and drag seen over the angle-of-attack sweep compared to the 5% x/c tripped case. At the post pitch-break angles-of-attack, the HRLES shows better agreement with the 25% x/c tripped case while URANS shows an underprediction. At the pre pitch-break angles-of-attack, both URANS and HRLES show higher lift. There is relatively little sensitivity to increasing mesh resolution for HRLES when observing the lift and drag curves. However, with increasing mesh resolution, the pitching-moment shows better agreement with the 5% x/c tripped case.
2) Both URANS and HRLES predict the shock developing further downstream when compared to the experiment as observed in the surface pressure curves at the pre pitch-break angles-of-attack (*i.e.* $\alpha < 3.0°$). HRLES shows an improved prediction of the shock location with grid refinement at the angles-of-attack post pitch-break. However, there is a plateau in the pressure immediately behind the shock and subsequently an underprediction in pressure rise in the downstream development to the trailing edge. This corresponds to larger regions of separated flow predicted by HRLES, compared to URANS, that were observed in the skin friction coefficient contours. The plateaued region is reduced with grid refinement and beginning at the trailing edge, the prediction of the pressure

improves. HRLES shows superior predictions of the overall surface pressure on the upper surface of the wing when compared to URANS at the higher angles-of-attack such as $\alpha = 5.0^\circ$ and $\alpha = 6.0^\circ$.

3) The onset of buffet appears to originate in the mid-span region of the main wing based on the instantaneous surface pressure contours and the PSD data. HRLES shows generally good agreement with the PSD data, particularly in the frequency range that is associated with transonic buffet instability modes. The excessive separation predicted by HRLES is observable in the spectra by higher amplitude content at the higher frequency range. Although not shown in the paper, the PSD levels in this higher frequency range are reduced with increasing mesh resolution. This also corresponds to what was observed in the surface pressure data. URANS tends to overpredict the peak PSD value when compared to experiment and shows a faster decay at higher frequencies. It appears that both HRLES and URANS predict the onset of buffet at around 0.5° earlier than the experiment, based on the PSD curves. HRLES performs particularly well at tracking the PSD spectra across the frequency range for $\alpha < 4.0^\circ$. The HRLES indicates some shock boundary-layer interaction in the wing-strut channel that is not consistent to what is measured in the experiment. Further testing of the CFD in an in-tunnel configuration will be needed to determine if this is a model error or due to the tunnel environment (*i.e.* floor boundary layer, blockage effects *etc*), or an aeroelastic effect.

Further work is required to determine if when moving to finer grids, HRLES will continue to improve the agreement of the predictions compared to the experiment with regards to reducing the separated flow region. A high fidelity model of the in-tunnel environment will also be needed to compare with the uncorrected in-tunnel angles-of-attack and if buffet can be predicted under those conditions. Finally, during the experiment, at some of the higher angles-of-attack there was observable flutter particularity in the outboard region of the wing which is not modeled in the simulations presented in this paper. Incorporating fluid-structure interaction methods into these simulations and running CFD simulations on static deformed girds will be another area of research that will be investigated.

Acknowledgments

This work was funded by the NASA Advanced Air Transport Technology (AATT) Project. Computer time has been provided by the NASA Advanced Supercomputing (NAS) facility at NASA Ames Research Center. The authors appreciated the help of Gregory Zilliac (NASA Ames) and Max Amaya (NASA Ames) with obtaining and discussing the experimental data. The authors also appreciated the help of Leonardo Machado (NASA Ames) with reviewing this paper and Francois Cadieux (NASA Ames) with both reviewing this paper and many fruitful discussions. The authors also thank Gerrit Stich (NASA Ames) for providing help with post-processing some of the data.

References

[1] Rumsey, C. L., Slotnick, J. P., and Woeber, C. D., "Fourth High-Lift Prediction/Third Geometry and Mesh Generation Workshops: Overview and Summary," *Journal of Aircraft*, Vol. 60, No. 4, 2023, pp. 1160–1177. doi:10.2514/1.C037168.

[2] Ghate, A. S., Kenway, G. K. W., Stich, G.-D., Maldonado, D., and Kiris, C. C., "A Wall-Modeled LES Perspective for the High Lift Common Research Model Using LAVA," *AIAA Aviation 2022 Forum,* AIAA Paper 2022-3434, 2022. doi:10.2514/6.2022-3434.

[3] Goc, K., Bose, S. T., and Moin, P., "Large Eddy Simulation of the NASA High-Lift Common Research Model," *AIAA SciTech 2022 Forum,* AIAA Paper 2022-1556, 2022. doi:10.2514/6.2022-1556.

[4] Kiris, C. C., Ghate, A. S., Browne, O. M. F., Slotnick, J., and Larsson, J., "HLPW-4: Wall-Modeled Large-Eddy Simulation and Lattice–Boltzmann Technology Focus Group Workshop Summary," *Journal of Aircraft*, Vol. 60, No. 4, 2023, pp. 1118–1140. doi:10.2514/1.C037193.

[5] Browne, O. M. F., Housman, J. A., Kenway, G. K., Ghate, A. S., and Kiris, C. C., "Numerical Investigation of CL,max Prediction on the NASA High-Lift Common Research Model," *AIAA Journal*, Vol. 61, No. 4, 2023, pp. 1639–1658. doi:10.2514/1.J062508.

[6] Mauery, T., Alonso, J., Cary, A., Lee, V., Malecki, R., Mavriplis, D., Medic, G., Schaefer, J., and Slotnick, J., "A Guide for Aircraft Certification by Analysis," NASA CR-20210015404, NASA, 2021.

[7] Balakumar, P., Iyer, P. S., and Malik, M. R., "Turbulence Simulations of Transonic Flows over an NACA-0012 Airfoil (Invited)," *AIAA SCITECH 2023 Forum,* AIAA Paper 2023-0254, 2023. doi:10.2514/6.2023-0254.

[8] Deck, S., "Numerical simulation of transonic buffet over a supercritical airfoil," *AIAA Journal*, Vol. 43, No. 7, 2005, pp. 1556–1566. doi:10.2514/1.9885.

[9] Grossi, F., Braza, M., and Hoarau, Y., "Prediction of transonic buffet by delayed detached-eddy simulation," *AIAA Journal*, Vol. 52, No. 10, 2014, pp. 2300–2312. doi:10.2514/1.J052873.

[10] Fukushima, Y., and Kawai, S., "Wall-modeled large-eddy simulation of transonic airfoil buffet at high Reynolds number," *AIAA Journal*, Vol. 56, No. 6, 2018, pp. 2372–2388. doi:10.2514/1.J056537.

[11] Ghate, A. S., Kenway, G. K., Stich, G.-D., Browne, O. M., Housman, J. A., and Kiris, C. C., "Transonic lift and drag predictions using Wall-Modelled Large Eddy Simulations," *AIAA SciTech 2021 Forum,* AIAA Paper 2021-1439, 2021. doi:10.2514/6.2021-1439.

[12] Tamaki, Y., and Kawai, S., "Wall-modeled LES of transonic buffet over NASA-CRM using Cartesian-grid-based flow solver FFVHC-ACE," *AIAA SciTech 2023 Forum,* AIAA Paper 2023-0429, 2023. doi:10.2514/6.2023-0429.

[13] Goc, K., Agrawal, R., Moin, P., and Bose, S., "Studies of transonic aircraft flows and prediction of initial buffet onset using large-eddy simulations," *AIAA Aviation 2023 Forum,* AIAA Paper 2023-4338, 2023. doi:10.2514/6.2023-4338.

[14] Ehrle, M., Waldmann, A., Lutz, T., and Krämer, E., "Simulation of transonic buffet with an automated zonal DES approach," *CEAS Aeronautical Journal*, Vol. 11, 2020, pp. 1025–1036. doi:10.1007/s13272-020-00466-7.

[15] Sartor, F., and Timme, S., "Delayed Detached–Eddy Simulation of Shock Buffet on Half Wing–Body Configuration," *AIAA Journal*, Vol. 55, No. 4, 2017, pp. 1230–1240. doi:10.2514/1.J055186.

[16] Spalart, P. R., Deck, S., Shur, M. L., Squires, K. D., Strelets, M. K., and Travin, A., "A new version of detached-eddy simulation, resistant to ambiguous grid densities," *Theoretical and Computational Fluid Dynamics*, Vol. 20, No. 3, 2006, p. 181. doi:10.1007/s00162-006-0015-0.

[17] Deck, S., and Renard, N., "Towards an enhanced protection of attached boundary layers in hybrid RANS/LES methods," *Journal of Computational Physics*, Vol. 400, 2020, p. 108970. doi:10.1016/j.jcp.2019.108970.

[18] Kiris, C. C., Housman, J. A., Barad, M. F., Brehm, C., Sozer, E., and Moini-Yekta, S., "Computational framework for launch, ascent, and vehicle aerodynamics (LAVA)," *Aerospace Science and Technology*, Vol. 55, 2016, pp. 189–219. doi:10.1016/j.ast.2016.05.008.

[19] Deck, S., "Recent improvements in the zonal detached eddy simulation (ZDES) formulation," *Theoretical and Computational Fluid Dynamics*, Vol. 26, No. 6, 2012, pp. 523–550. doi:10.1007/s00162-011-0240-z.

[20] Browne, O. M. F., Housman, J. A., Kenway, G. K. W., Ghate, A. S., and Kiris, C. C., "A Hybrid RANS-LES Perspective for the High Lift Common Research Model Using LAVA," *AIAA Aviation 2022 Forum,* AIAA Paper 2022-3523, 2022. doi:10.2514/6.2022-3523.

[21] Housman, J. A., Stich, G.-D., Kocheemoolayil, J. G., and Kiris, C. C., "Predictions of Slat Noise from the 30P30N at High Angles of Attack using Zonal Hybrid RANS-LES," *25th AIAA/CEAS Aeroacoustics Conference,* AIAA Paper 2019-2438, 2019. doi:10.2514/6.2019-2438.

[22] Stich, D., Housman, J. A., Kocheemoolayil, J. G., Barad, M. F., Cadieux, F., and Kiris, C. C., "Application of Lattice Boltzmann and Navier-Stokes Methods to NASA's Wall Mounted Hump," *2018 Fluid Dynamics Conference,* AIAA Paper 2018-3855, 2018. doi:10.2514/6.2018-3855.

[23] Spalart, P., and Allmaras, S., "A one-equation turbulence model for aerodynamic flows," *30th Aerospace Sciences Meeting and Exhibit,* AIAA Paper 1992-439, 1992. doi:10.2514/6.1992-439.

[24] Allmaras, S. R., and Johnson, F. T., "Modifications and clarifications for the implementation of the Spalart-Allmaras turbulence model," *Seventh International Conference on Computational Fluid Dynamics (ICCFD7)*, Vol. 1902, Big Island, HI, 2012.

[25] Spalart, P. R., and Garbaruk, A. V., "Correction to the Spalart–Allmaras Turbulence Model, Providing More Accurate Skin Friction," *AIAA Journal*, Vol. 58, No. 5, 2020, pp. 1903–1905. doi:10.2514/1.J059489.

[26] Spalart, P., "Trends in turbulence treatments," *Fluids 2000 Conference and Exhibit*, 2000. doi:10.2514/6.2000-2306.

[27] Crouch, J., Garbaruk, A., Magidov, D., and Travin, A., "Origin of transonic buffet on aerofoils," *Journal of Fluid Mechanics*, Vol. 628, 2009, p. 357.

[28] Stich, G.-D., Housman, J. A., Kocheemoolayil, J. G., Kiris, C. C., and Bridges, J. E., "Large-Eddy Simulation of Jet Surface Interaction Noise," *25th AIAA/CEAS Aeroacoustics Conference,* AIAA Paper 2019-2475, 2019. doi:10.2514/6.2019-2475.

[29] Housman, J. A., Stich, G.-D., and Kiris, C. C., "Jet noise prediction using hybrid RANS/LES with structured overset grids," *23rd AIAA/CEAS Aeroacoustics Conference,* AIAA Paper 2017-3213, 2017. doi:10.2514/6.2017-3213.

[30] Brehm, C., Barad, M. F., Housman, J. A., and Kiris, C. C., "A comparison of higher-order finite-difference shock capturing schemes," *Computers & Fluids*, Vol. 122, 2015, pp. 184–208. doi:10.1016/j.compfluid.2015.08.023.

[31] Shu, C.-W., "High order weighted essentially nonoscillatory schemes for convection dominated problems," *SIAM review*, Vol. 51, No. 1, 2009, pp. 82–126. doi:10.1137/070679065.

[32] Deng, X., and Zhang, H., "Developing high-order weighted compact nonlinear schemes," *Journal of Computational Physics*, Vol. 165, No. 1, 2000, pp. 22–44. doi:10.1006/jcph.2000.6594.

[33] Deng, X., "New high-order hybrid cell-edge and cell-node weighted compact nonlinear schemes," *20th AIAA Computational Fluid Dynamics Conference,* AIAA Paper 2011-3857, 2011. doi:10.2514/6.2011-3857.

[34] Nonomura, T., and Fujii, K., "Robust explicit formulation of weighted compact nonlinear scheme," *Computers & Fluids*, Vol. 85, 2013, pp. 8–18. doi:10.1016/j.compfluid.2012.09.001.

[35] Wong, M. L., and Lele, S. K., "High-order localized dissipation weighted compact nonlinear scheme for shock-and interface-capturing in compressible flows," *Journal of Computational Physics*, Vol. 339, 2017, pp. 179–209. doi:10.1016/j.jcp.2017.03.008.

[36] Thornber, B., Mosedale, A., Drikakis, D., Youngs, D., and Williams, R. J., "An improved reconstruction method for compressible flows with low Mach number features," *Journal of Computational Physics*, Vol. 227, No. 10, 2008, pp. 4873–4894. doi:10.1016/j.jcp.2008.01.036.

[37] Harten, A., Lax, P. D., and Leer, B. v., "On upstream differencing and Godunov-type schemes for hyperbolic conservation laws," *SIAM review*, Vol. 25, No. 1, 1983, pp. 35–61. doi:10.1007/978-3-642-60543-7_4.

[38] Kiris, C. C., Ghate, A. S., Duensing, J. C., Browne, O. M., Housman, J. A., Stich, G.-D., Kenway, G., Dos Santos Fernandes, L. M., and Machado, L. M., "High-Lift Common Research Model: RANS, HRLES, and WMLES perspectives for CLmax prediction using LAVA," *AIAA SciTech 2022 Forum,* AIAA Paper 2022-1554, 2022. doi:10.2514/6.2022-1554.

[39] Harrison, N. A., Gatlin, G. M., Dickey, E. D., and Malone, A. M., "Transonic Truss-Braced Wing Vision Vehicle Technology Maturation," *ICAS 2022,* Paper 2022-0397, 2022.

[40] Harrison, N. A., Sclafani, A. J., Cerra, D., Dickey, E. D., Patel, D., Straccia, J., Vijgen, P., Crouch, J., Otto, C., Loh, K.-C., and Jones, A., "Subsonic Ultra Green Aircraft Research: Phase V - Buffet Test Report," NASA CR–2023-XXXXXX, NASA, 2023.

[41] Sleppy, M., Engel, E., Watson, K., and Atler, D., "Investigation of Seal-to-Floor Effects on Semi-Span Transonic Models," *47th AIAA Aerospace Sciences Meeting,* AIAA Paper 2009-619, 2009. doi:10.2514/6.2009-619.

[42] Délery, J., and Bur, R., "The physics of shock wave/boundary layer interaction control: last lessons learned," *Office National d Etudes ET DE Recherches Aerospatiales Onera-Publications-Tp*, Vol. 181, 2000.

[43] Maldonado, D., Viken, S. A., Housman, J. A., Hunter, C. A., Duensing, J. C., Frink, N. T., Jensen, J. C., McMillin, S. N., and Kiris, C. C., "Computational Simulations of a Mach 0.745\Transonic Truss-Braced Wing Design," *AIAA SciTech 2020 Forum,* AIAA Paper 2020-1649, 2020. doi:10.2514/6.2020-1649.

[44] Maldonado, D., Hunter, C., Housman, J. A., Viken, S. A., Piotrowski, M. G., McMillin, S. N., Kiris, C. C., and Milholen, W. E., "Improvements in Simulating a Mach 0.80 Transonic Truss-Braced Wing Configuration using the Spalart-Allmaras and k-ω SST Turbulence Models," *AIAA SciTech 2021 Forum,* AIAA Paper 2021-1531, 2021. doi:10.2514/6.2021-1531.

[45] Ghate, A. S., Housman, J. A., Stich, G.-D., Kenway, G., and Kiris, C. C., "Scale resolving simulations of the NASA Juncture Flow Model using the LAVA solver," *AIAA Aviation 2020 Forum,* AIAA Paper 2020-2735, 2020. doi:10.2514/6.2020-2735.

[46] Amaya, M. A., and Richey, C. S., "Background Acoustic Characteristics of the NASA Ames 11-by 11- Foot Transonic Wind Tunnel," Tech. rep., Wind Tunnel Operations Branch, NASA Ames Research Center, Nov. 2008.